Submarine Landslides & Tsunami

Nikos Kalligeris

Department of Environmental Engineering

Technical University of Crete

A thesis submitted for the degree of

Master of Science (MSc)

January 2010

Abstract

This thesis is an introduction to marine geotechniques and submarine landslide-generated tsunami. It can serve as a tool for engineers assessing underwater slope stability and evaluating coastal hazard from submarine landslide-generated tsunamis. It covers a wide range of topics, from basic soil mechanics concepts to underwater slope stability analysis. Also, information on marine soil characteristics and mechanical properties is given to provide an engineer with a set of representative values of common soil properties. In the last chapter, an introduction is given to tsunami, covering earthquake and landslide-generated tsunami initial conditions. For landlside-generated tsunami, empirical formulae available in literature, to generate one, two and three-dimensional surface waveforms are discussed.

Contents

Chapter 1

Introduction

Underwater landslides are part of the broader family of landslides. As the name implies, underwater (same as submarine) landslides occur under water, which affects both failure initiation characteristics and post-failure evolution and dynamics. Submarine landslides occur frequently on both passive and active continental margins, especially on the continental slopes, where storm waves and earthquakes are the major cause of landslides, but can also occur in fjords where rapid deposition of sediments is the main trigger [128],[83]. The size of the slides occurring under water is typically larger than for subaerial slides, 105 to 1011 m^3 in terrestrial, subaerial settings and up to 1013 m^3 for submarine landslides [63], with the largest submarine landslide reported being the Agulhas slide off South Africa, which involved a volume as large as 20,000 km3 [21]. Also submarine landslides are much more mobile than subaerial slides; displaced masses can travel vast distances downslope until they encounter seamounts or gentler slopes and get deposited. The larger associated runout distances are a direct consequence of the fact that the material is mixed with large amounts of water [63]. Note that runout distances of more than 800 km have been reported as for the Storegga slide located on the Norwegian continental margin [12].

But why would we be interested in submarine landslides, except for scientific reasons of course? There is a growing development of offshore activities along margins, mainly marine oil platforms and also offshore installations such as cables and pipelines that are laid on the sea-bottom that are threatened by the forces arising from submarine masses which can travel at speeds as high as 108km/h (30m/s) [128]. In addition, submarine landslides often give rise to tsunami that threaten offshore infrastructure as well as coastal areas and ships in the vicinity of the mass failure initiation. Production from offshore fields in areas with earlier sliding activity is ongoing in the Norwegian margin, Gulf of Mexico, offshore Brazil, the Caspian Sea and West Africa [83]. Damage to or collapse of a wharf or pier, carrying oil may results in an oil spill which can have a big environmental impact and pose health concerns as well as big economic losses, as the cost of cleaning up oil spills in waterways can range from $ 10,000/bbl up to $ 250,000/bbl [27]. Therefore due to the ecologic, economic and life threatening consequences, the study of this natural disaster is essential to understand how this phenomenon is triggered, the physics behind the post-failure evolution downslope, the coupling of submarine slide and the tsunami that can possibly be generated, to assess risk associated with submarine landslides and be prepared for future events.

Chapter 2

Basic Soil Mechanics concepts

In this chapter basic soil mechanics concepts are covered to provided the basis of the analysis that follows.

2.1 Shear Strength

The *shear strength* of the soil, at any point on a particular plane is most commonly determined from the so-called Mohr-Coulomb failure criterion:

$$s = c + \sigma \tan \phi \tag{2.1}$$

where s is the shear strength, c and ϕ are the *shear strength parameters*, namely *cohesion intercept* (or cohesion) and *angle of shearing resistance* (or *angle of internal friction*, or *friction angle*), is the *total normal stress* and u is the *pore water pressure.*

Terzaghi's ([121], [122], [123]) fundamental concept, first introduced in 1936 at the first Conference on Soil Mechanics and Foundation Engineering, states that shear stress in a soil can be resisted only by the skeleton of solid particles. For *fully saturated* soils a change in pore water pressure $u$produces practically no volume change (water is considered as incompressible) and has practically no influence on the stress conditions for failure [85]. Expressing eq. 2.1 in terms of *effective shear stress* leads to:

$$s = c' + (\sigma - u) \tan \phi' \tag{2.2}$$

where c' and $\phi'$are the *shear strength parameters* in terms of effective stress and

$$\sigma' = (\sigma - u) \tag{2.3}$$

represents the *effective normal stress* (σ').

The principle of effective stress is illustrated in (figure 2.1): A plane XX in a fully saturated soil is passing through the particle points of contact. The normal force P applied over the area A will be resisted partly by inter-particle forces and partly by the pore water pressure. Inter-particle forces being random in direction and magnitude can be split in two components: N and T the normal to A and normal to XX planes respectively. The effective stress will be the sum of forces N over the area A ($\sigma = \sum N/A$) and the total stress will be the force P over A ($\sigma = P/A$). The pore water pressure will act on the entire area A, since point contact is assumed between soil particles. Equilibrating forces in the direction normal to plane XX leads to:

$$P = \sum N' + uA \Rightarrow \frac{P}{A} = \frac{\sum N'}{A} + u \Rightarrow \sigma = \sigma' + u \tag{2.4}$$

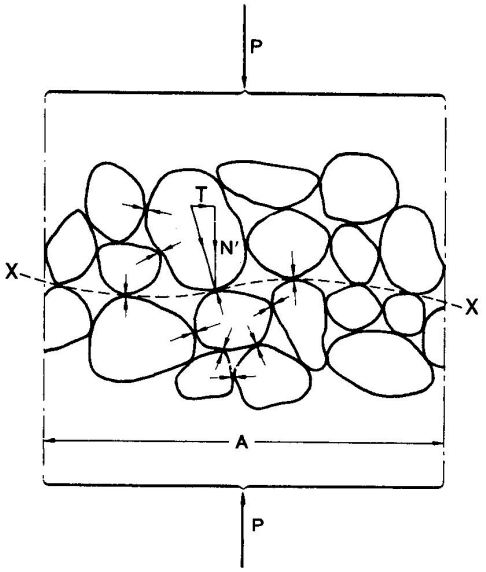

Figure 2.1: Interpretation of effective stress (after Craig [13])

It was actually Coulomb [15] who first introduced eq. 2.1 and Mohr's contribution came later. Coulomb determined that the soil and rock shear strengths are the sum of two components, one due to a constant cohesion, the other due to a friction strength dependent on the normal stress acting on the plane on which the shear strength is mobilized [36]. Mohr developed the more generalized form of the equation by expressing the shear strength in terms of the effective major and minor principal stresses σ_1' and σ_3' at failure at the point in question.

At failure, the straight line represented by eq. 2.2 defines the upper stress limit, and thus will be tangetial to the Mohr circle representing the state of stress as shown in figure 2.2.

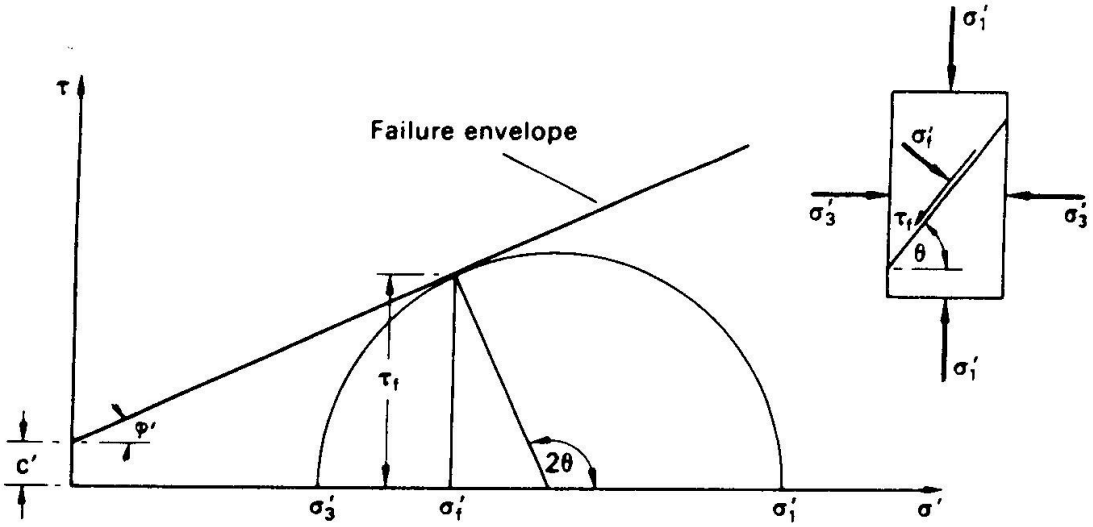

Figure 2.2: Stress conditions at failure (after Craig [13]).

From fig. 2.2, shear and effective normal stress at failure are given by:

$$P = \sum N' + uA \Rightarrow \frac{P}{A} = \frac{\sum N'}{A} + u \Rightarrow \sigma = \sigma + u \tag{2.5}$$

where θ is the theoretical angle between the major principal and the failure plane.

From geometry it is apparent that:

$$\theta = 45\,\text{deg} + \frac{\phi'}{2} \tag{2.6}$$

Given that the radius of the Mohr cirlcle is $(\sigma_1 - \sigma_3,)/2$, taking the sine of angle ϕ' leads to

$$\sin(\phi') = \frac{\frac{1}{2}\,(\sigma_1' - \sigma_3')}{c'\phi' + \frac{1}{2}\,(\sigma_1' + \sigma_3')} \tag{2.7}$$

which equation is referred to as the Mohr-Coulomb criterion. Given a number of stress states at failure one can plot the Mohr circles in a $\tau - \sigma$axis plot and find the common tangent to the circles which will represent the *failure envelope*.

2.1.1 Saturated vs partially saturated soil

The difference between saturated and unsaturated soil is the percentage of water content in the voids of the soil column. The *degree of saturation* is defined as the ratio of volume of water to the total volume of void space:

$$S_r = \frac{V_w}{V_s} = \frac{wG_s}{e} \tag{2.8}$$

where V_v is the total volume of void space V_w is the volume of water, w is the *water content* ($w = M_m/M_s$, mass of water over the mass of solids), G_s is the *specific gravity* of the soil particles ($G_s = \rho_s/\rho_w$, particle density over density of water) and e is the *void ratio* ($e = V_0/V_s$, volume of voids over total volume of soil). The degree of saturation can range between 0% ($S_r = 0$) for a completely dry soil, to 100% ($S_r = 1$) for a fully saturated soil.

Consider the case of a fully saturated soil and a case of partially saturated soil, both subject to an increase in total vertical stress. Assume that lateral strain in confined: volume change being allowed only in the vertical direction (this assumption is valid when the load is applied on an area large compared with the thickness of the soil layer).

Saturated soil. Initially, the water table is at the surface of the soil, with pore water pressure being constant and equal to the static value ($u = u_s$). When the load is applied and the total stress is increased, the soil particles try to re-arrange and take new positions. However, the void ratio is zero (voids being filled with water), and the soil is laterally confined. Therefore no particle rearrangement is possible if the water is not allowed to escape, or in other words if no *drainage* is allowed. In the *undrained* case, the entire extra load will be taken up by the water column resulting in an increase in pore water pressure, above the static value called excess pore pressure ($u = u_s + u_e$). Inter-particle forces will remain constant and thus effective stress is constant. In the *drained* condition, excess pore water pressure will slowly dissipate by seepage depending on the permeability of the soil, and when it's complete the soil skeleton will take the increment of total vertical stress. This process is referred to as *consolidation.*

Partially saturated soil. In partially saturated soils, part of the voids is filled with water and part with air, the water being considered as incompressible and the air as highly compressible. Unless the degree of saturation is close to unity, the air in the voids usually forms continues

channels through the soil skeleton, whereas water is concentrated around the soil [13]. In 1955 Bishop [3] proposed the following relationship between total and effective stress:

$$\sigma = \sigma' + u_a - \chi(u_a - u_w) \tag{2.9}$$

where u_a is the pore air pressure and χ is the a parameter related primarily to the degree of saturation of the soil.

2.1.2 Consolidation

As it was explained in the previous example of a fully saturated soil subject to an increase in total vertical stress, *consolidation* is the gradual reduction in volume of a fully saturated soil of low permeability due to drainage of some of the pore water, the process continuing until the excess pore water pressure set up by the increase in total stress has completely dissipated [13]. The opposite of *consolidation*, which is termed *swelling,* is the gradual increase in volume due to reduction of total vertical stress and negative excess pore water pressure. If the present effective stress is the maximum to which the soil has ever been subjected, then the soil is said to be *normally consolidated,* else if at some point in the past the effective stress has been greater than the present value, then the soil is said to be *over consolidated.* The maximum effective stress in the past over the maximum present value is defined as the *overconsolidation ratio*: $OCR = \sigma'_{vc}/\sigma'_{v0}$, where σ'_{vc} is the pre-consolidation pressure and σ'_{v0} is the present effective overburden pressure. The incompletely consolidated state is termed as *under consolidated* or just *incomplete consolidation.* In general, sediments on the continental shelf and the continental slope are in an overconsolidated state, deltaic deposits are incompletely consolidated, and abyssal plain deposits are normally consolidated (Fukuoka & Nakase 1973, referred in [92]).

Depending on the level of consolidation *(OCR)*, the shear strength parameters of the soil/sediment and the shear strength behavior under loading are different. In consolidated-undrained tests in the triaxial apparatus (an all-around pressure $(\sigma_1 - \sigma_3)$ (through water) is applied until consolidation is complete and then drainage is stopped and the principal stress difference $(\sigma_1 - \sigma_3)$ is applied unlit failure) for normally consolidated specimens, pore water pressure increases steadily during shearing, where for overconsolidated specimens pore water pressure increases initially and then decreases, sometimes reaching negative values in the case of heavily overconsolidated specimens. In consolidated-drained tests in the triaxial apparatus (an all-around pressure $(\sigma_1 - \sigma_3)$ (through water) is applied until consolidation is complete and then drainage is still allowed while the principal stress difference $(\sigma_1 - \sigma_3)$ is applied unlit failure) normally consolidated specimens fail in greater strains than overconsolidated specimens, the former showing strain-hardening effects and the later failing in a more abrupt way after a well formed peak.

2.1.3 Mechanisms of overconsolidation

For terrestrial soil, overconsolidation is usually the result of geological factors such as the erosion of overburden, the melting of ice sheets after glaciation and the permanent rise of the water table [13]. Under marine conditions the removal of overburden may rise from marine erosion in shallow water and from the effects of prior glaciation [92]. Also it may arise from prior wave action, especially in shallow waters [92]. Other non-mechanical processes of overconsolidation for marine sediments include [92]:

- Creep or secondary consolidation. It leads to a reduction in void ratio at constant effective stress and thus constitutes a pre-consolidation pressure.

- Cementation, which is the development of chemical bonding by precipitation of cementing agents.
- Trioxtropic hardening, which results in an increase in strength with time at constant composition.

2.1.4 Mechanisms of incomplete consolidation

Incomplete consolidation or *under consolidation* is not the opposite of *over consolidation*, it just means that the soil still has excess pore water pressure that has not been dissipated. Mechanisms of *under consolidation* include:

[**a**] Rapid rates of sedimentation. High rates of sedimentation induce rise of pore water pressure, and if excess pore water pressure is not dissipated at the same pace as it is induced, then the soil remains *under consolidated* [92].

[**b**] Gas in marine sediments. Either dissolved in pore water or in the form of free gas, the presence of gas in marine sediments increases the *in-situ* pore water pressure and the soil compressibility.

[**c**] Leakage from an artesian water of gas pressure source. Petroleum and water-bearing formations may be subject to pressures above hydrostatic and therefore have the tendency to flow towards a lower pressure environment. In the case of permeable soil layer overlaying and artesian source, leakage of water of gas can lead to the increase of pore water pressure. The excess pore water pressure will be maximum on the boundary between the soil layer and the artesian source and will decay linearly towards the top of the soil layer.

[**d**] Wave-induced repeated loading. Large storm wave can cause significant levels of cyclic stress in the upper parts of a soil layer and, in some soft saturated soils, it can lead to the generation of excess pore water pressure [92]. If the excess pore water pressure induced from a storm event is not dissipated until the next storm strikes again, it is possible that pore water pressure will be building up, leaving the soil layer in an *under consolidated* state. However, it is also possible that excess pore water pressure is dissipated during and after a storm event, being *over consolidated* after the storm event.

Mechanisms (a), (b) and (d) will be discussed in more detail in the slope stability section of this thesis.

Chapter 3

Nature of submarine soils

3.1 General characteristics

Marine sediment is a mixture of material from land, transported to the sea through rivers, glaciers and wind and substances extracted from biological or chemical processes [92]. Main differences between terrestrial and marine sediments include [92]:

- Ocean sediments are saturated with saline pore water.
- The composition of ocean sediments may differ from the terrestrial because of the biogenous particles present.
- The rate of deposition is usually much slower, especially in the deep sea.
- The high-pressure, low-temperature environment of ocean sediments may affect their microstructure.

There are two ways of classifying marine sediments: (i) by size or (ii) by origin. An example of classification by size is given in table 3.1.

Table 3.1: Classification of sediment particles by size (Wentworth scale, after Poulos [92]

Size fraction	Particle Diameter (mm)
Boulders	> 256
Cobbles	64 – 256
Pebbles	4 – 16
Granules	2 – 4
Sand	0.062 – 2
Silt	0.004 – 0.062
Clay	< 0.004

Classification by origin leads to three groups [92]:

- **Lithogenous particles:** primarily silicate mineral grains derived from the breakdown of silicate terrigenous rocks during weathering; volcanoes may also be sources of lithogenous particles.
- **Biogenous particles:** the insoluble remains of bones, teeth or shells of marine organisms.

- **Hydrogenous particles:** formed by chemical reactions occurring in seawater or within the sediments.

Lithogenous particles are the largest source of sediment in the ocean [92]. The finer-grained lithogenous sediments are frequently referred to as brown clays, because of their color, and contain clay minerals which may constitute 60% or more of the non-biogenous fraction [92]. Differences with terrestrial clays exist in terms of in-situ stress state and the possible presence of gases in the marine deposits [92]. However, there is evidence that the fundamental behavior of marine and terrestrial clays is similar, and that some of the correlations which have been derived for the engineering properties of terrestrial clays may be applied to marine deposits [92]. Lithogenous sediments will be referred from now on as inorganic clay and the behavior in terms of shear strength will be discussed in the next section.

Biogenous particles sediments can be either calcareous or siliceous in composition. The most common biogenous particles are calcareous, which are usually either shells or tests of foraminifera [92]. On the other hand, siliceous organisms include diatoms, radiolarians, sponges and silicoflagellates [92]. Calcareous sediments are commonly found in latitudes between 30^oN and 30^oS whereas siliceous are found mainly at high latitudes and in the equatorial Pacific [92]. In this thesis only calcareous sediments will be considered and their shear strength properties will be discussed in the next section.

More information about lithogenous and biogenous particles can be found in Poulos [92].

3.2 Shear strength of soil/sediments

3.2.1 Inorganic clay

Due to sampling disturbance, *in-situ* and laboratory undrained shear strength results deviate significantly and a method know as *SHANSEP* (*S*tress *H*istory *a*nd *N*ormalised *S*oil *E*ngineering *P*roperties) was introduced by Ladd & Foott [59]. In this approach, the normalized soil parameter (NSP), which is the measured undrained shear strength normalized with respect to the effective overburden pressure, provides a convenient framework for expressing sediment shear strength as a function of stress history and fundamental properties that are independent of the stress state.

Other techniques include the *recompression technique*, described by Bjerrum [7]. In this approach specimens are consolidated in laboratory at the same pressures to whicsh they were consolidated in the field, whereas in the *SHANSEP* technique samples are consolidated to effective stresses higher than the *in-situ* stresses [23]. The *recompression technique* is extensively used in Norway to evaluate undrained strengths of the sensitive marine clays found there [23]. Both techniques have limitations, the *recompression technique* being used for block samples of very little disturbance and the *SHANSEP* technique is used in clays for which undrained strength increases in direct proportion to the consolidation pressure [23].

For normally consolidated clays, normalized shear strength s_u/σ'_{v0} has been shown to increase with increasing plasticity index (Bjerrum & Simons [6]), the relation being almost a straight line. Significant deviations from this trend suggest the presence either of diagenetic bonding (cementation) and associated strength gain, or under-consolidation with associated strength loss [28]. For overconsolidated clays, there is a unique relationship between OCR and the ratio of the normalized shear strength for overconsolidation and normally consolidated clays that can be approximated as [92]:

$$(s_u/\sigma_v 0')_o c/(s_u/\sigma'_{v0})_n c = (OCR)^m \tag{3.1}$$

where m is a soil constant (~ 0.8).

In terms of effective stress, normalized undrained strength can be expressed as:

$$\frac{s_u}{\sigma'_{v0}} = \frac{[K_0 + A_f(1-K_0)]\sin\phi' + (c'/\sigma'_{v0})\cos\phi'}{1 + (2A_f - 1)\sin\phi'} \tag{3.2}$$

where K_0 is the coefficient of earth pressure at rest, A_f is the pore pressure parameter (sometimes called *pore pressure coefficient* as well) A at failure, and $\sigma_v 0'$ is the initial vertical effective stress [92]. Effective stress cohesion c' is zero for normally consolidated clays and can approximated as such, unless the soil is cemented [92].

Pore pressure parameters are used to express the response of pore water pressure to changes in total stress under undrained conditions and enable the initial value of excess water pressure to be determined [13]. Skempton [109] defined the two pore pressure parameters A & B as:

$$\Delta u = B[\Delta\sigma_3 + A(\Delta\sigma_1 - \Delta\sigma_3)] \tag{3.3}$$

The parameter B depends on the degree of saturation and equals to 1 for fully saturated soils and 0 for dry soils. The pore pressure parameter A depends on the stress path to failure and can be determined experimentally from measurements of pore water pressure during the application of principal stress difference under undrained conditions in a triaxial test. Typical values for A_f are between 0.6 and 1.0 [92]. In Sarma & Jennings [101] parameters A_n are defined as a function of the number of cycles.

For normally consolidated clays, K_0 can be approximated by the Jacky [54] expression:

$$K_0 = 1 - \sin\phi' \tag{3.4}$$

whereas for overconsolidated clays, Mayne & Kulhawy [75] suggest that K_0 may be approximated as:

$$K_0 = (1 - \sin\phi')(OCR)^{\sin\phi'} \tag{3.5}$$

3.2.2 Calcareous sediments

Shear strength of calcareous sediments is usually expressed in terms of effective stress, however for fine-grained soils, it can also be expresses in terms of total stress to give the undrained shear strength. In the case of effective stress, it was found that there is a relationship between the effective stress angle of friction ϕ' and the mean effective stress p' (equal to $(\sigma'_1 + \sigma'_2 + \sigma'_3)/3$) that can be approximated well by [92]]:

$$\phi' = \alpha - b\log_{10} p' \tag{3.6}$$

The decrease of friction angle with increasing mean effective stress has been attributed by Datta *et al.* [18] to particle crushing.

Other factors affecting shear strength are cementation and carbonate content, the former showing beneficial effects up to strains of 0.5% and the later overall detrimental effects with friction angle decreasing with increasing carbon content.

Tables 3.2 and 3.3 show effective and undrained shear strength parameters of calcareous soils.

Table 3.2: Effect of carbonate content on strength parameters (Demars *et al.* [19])

Carbonate content	c' (kPa)	ϕ' (degrees)	A_f
0.25	0	27.7	0.7
25-40	0	29.4	0.55
40-60	0.7	31.7	0.40
>60	0.7	31.3	0.25

3.3 Soil behavior under cyclic loading

Soil behavior under cyclic loading can be examined either by numerical methods or the *critical state concept* introduced by Roscoe, Schofield & Wroth [97].The *critical state theory*, unifies the characteristics of shear strength and deformation by representing the state of stress of the soil at any time with the parameters *e, p* and *q*, where e is the void ratio, p is the mean effective stress $(\sigma'_1 - \sigma'_3)/3$ and q is the deviator stress $(\sigma'_1 - \sigma'_3)$. The concept was first introduced to idealize the behavior of remoulded clays in triaxial compression tests, but is is assumed to apply aslo to undistrurbed clays [13].

It was shown that a single, characteristic surface or line exists which uniquely defines the states of failure for a given soil called the *critical surface* (in three dimensions, *e, p* and *q*) and *critical state line* (two dimensions) respectively. When the *critical state* is reached, the soil will deform without changes of void ratio or state of stress. However, the state of failure of a soil is dependent on the stress history preceding failure, and hence a soil may have several *critical states.* For example, the *critical state line* obtained from consolidated-undrained and drained triaxial tests for normally consolidated clay may not be reached by specimens of heavily overconsolidated clay due to a tendency of heavily overconsolidated clays to increase in volume prior to and after failure. Of particular interest, are two states of failure appear to be independent of stress history. One is the *steady state* (SS), in which the soil deforms continuously at constant volume and constant effective stress and the other is the *cyclic limit state* (CLS) which is the failure state induced by cyclic loading (upper bound of non-failure behavior for very large number of cycles) introduced by Sangrey *et al.* [99].

In terms of cyclic loading behavior, soils can be divided in two categories: *contractive* soils and *dilative* soils. When loaded to failure (under cyclic loading) both *contractive* and *dilative* soils exhibit continuous increase in pore pressure or continuous decrease in void ratio (strain softening material), the difference being that *dilative* soils sometimes prior to failure tend to exhibit either decrease in pore water pressure or increase in void ratio (strain hardening material). *Contractive* and *dilative* soils are also termed as *collapsible* and *non-collapsible* soils respectively.

Figure 3.1 shows the stress paths of several types of triaxial tests on contractive and dilative soils. Path I represents an undrained compression test, which is characterized by an evident decrease in mean effective normal stress due to pore pressure increase until failure is reached on the steady state curve (point c). Path II is the stress path of an undrained compression test on a dilative soil. It can be seen that effective stress is increased due to the decrease of pore water pressure until point e is reached and then pore pressures rises until failure is reached on point f. Path III is for a typical drained compression test on a contractive soil where void ratio is reduced due to drainage. Finally path IV represents an undrained cyclic loading test of a saturated contractive soil, where pore pressure increases with each loading cycle until failure is reached at point k on the cyclic limit state. This is also illustrated in figure 3.2, where it is shown how strain builds up and pore water pressure rises after each loading cycle leading to

gradual loss of effective strength. When a soil losses its shear strength completely due to rise of pore water pressures, then the soil is said to *liquefy*. Loss of shear strength means loss of grain-to-grain contact, which can only happen in saturated cohesionless soils, for which true *liquefaction* can occur. However, in geotechnical engineering applications the term *liquefaction* does not necessarily mean complete loss of shear strength but just reduction of shear strength due to pore water pressure rise.

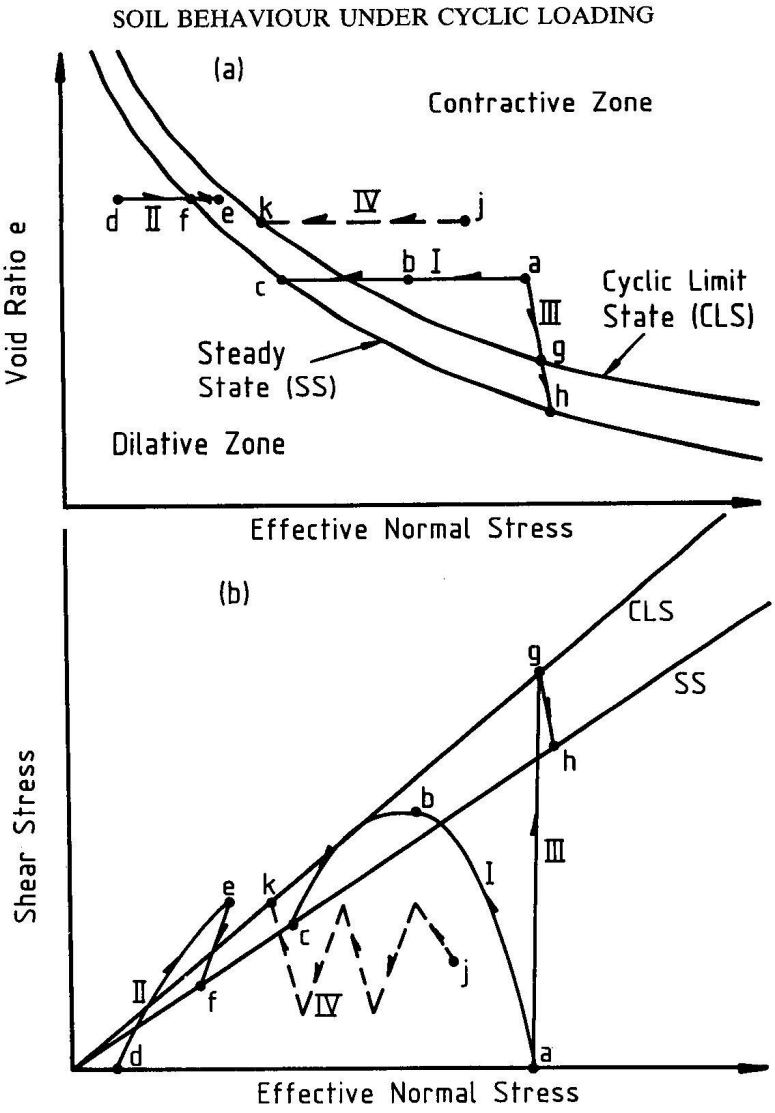

Figure 3.1: Perspectives of the state space with several test paths: (a) void ratio versus effective normal stress, and (b) shear stress versus effective normal stress (after Sangrey *et al.* [99]).

At this point it must be stressed that the behavior of a soil specimen under cyclic loading strongly depends on the level of cycled stress. At low levels of cyclic stress, limited amount of pore pressure develops and a non-failure equilibrium is reached in which strain and pore pressure return to the same values after each cycle of loading. The cyclic stress level that separates failure from equilibrium behavior is the critical level of repeated loading (CLRL, after Sangrey *et al.* [98]) [92].

Other important conclusions drawn from Sangrey *et al.* [99] include:

[**a**] The laboratory data indicates that the cyclic limit state coincides with the remoulded

strength state for clays and the steady state for sands.

[**b**] The behavior of sands and clays is fundamentally similar.

[**c**] Dissipation of residual positive pore pressures through drainage in contractive soils increases the CLRL and improves the response of the soil in cyclic loading.

[**d**] In general, dissipation of residual negative pore pressures through drainage in dilative soils lowers the undrained shear strength. Whether negative pore pressures will develop depends on the initial density of the soil, the initial overconsolidation ration and the magnitude of the applied cyclic stress [74].

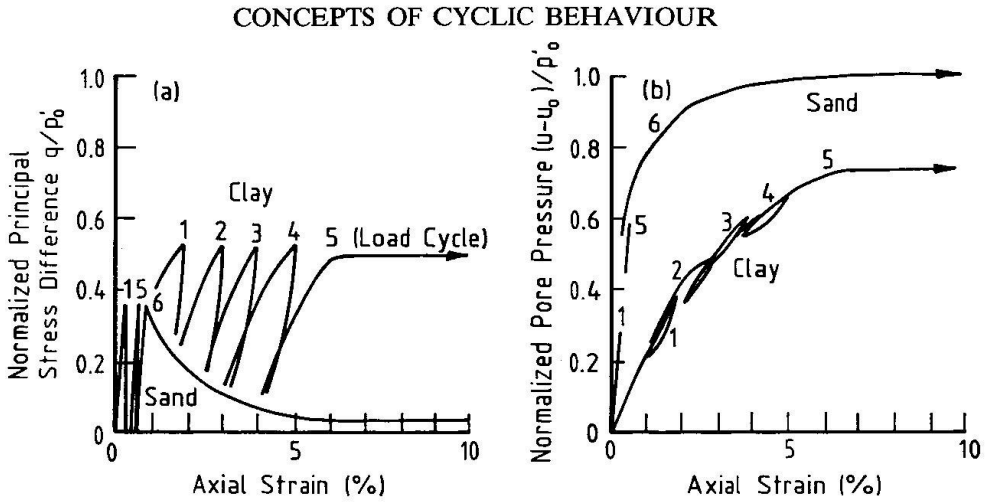

Figure 3.2: Cyclic loading of contractive specimens of sand and clays leads to failure when pore pressures increase sufficiently (after Sangrey *et al.* [98])

Evaluation of cyclic liquefaction potential

Many factors govern the liquefaction process for in situ soil and the most important are intensity of earthquake and its duration, location of ground water table, soil type, soil relative density, particle size gradation, particle shape, depositional environment of soil, soil drainage conditions, confining pressures, aging and cementation of the soil deposits, historical environment of the soil deposit and building/additional loads on these deposits (Sitharam *et al.* [108]). Soils most susceptible to liquefaction are sands with rounded particles, at very loose density state, recently deposited with no cementation between soil grains, and no prior preloading or seismic shaking (Sitharam *et al.* [108]).

Commonly employed approaches to evaluate liquefaction potential are the cyclic stress approach and the cyclic strain approach. To determine the stress conditions causing liquefaction of the soil, some approaches employ data from the field and in others data from laboratory tests. Laboratory tests include cyclic trialxial test, cyclic shear and cyclic torsional test. Some of the *in situ* tests include the Standard Penetration Test (SPT), Cone Penetration Test (CPT), shear wave velocity method and the dilatometer test. However, it should be noted that laboratory test are only valid for undisturbed samples and because of the difficulty of obtaining undisturbed samples it is generally preferred to adopt the field correlation approach (Seed *et al.* [107]).

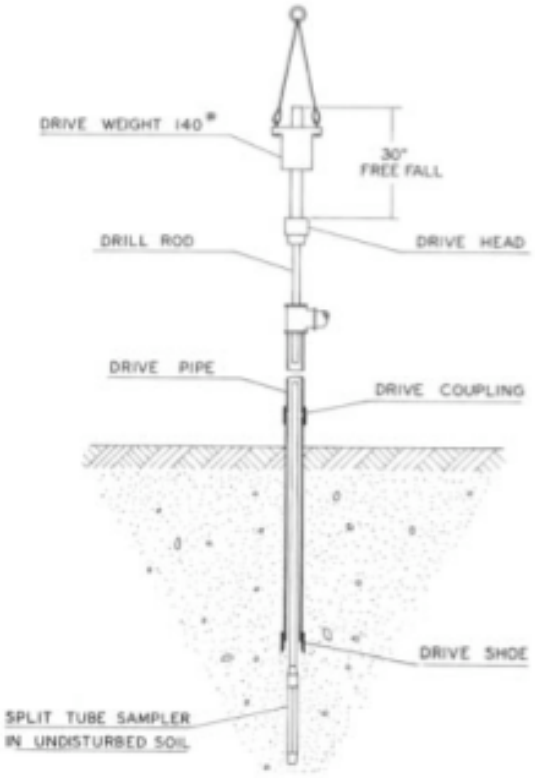

Figure 3.3: Components of SPT spilt spoon sampler (source: [142])

Most available data on field performance have been collected using the SPT. For that reason, it is also commonly used in semi-empirical methods of determining site liquefaction potential. The SPT has its origins in the 1900's where the owner (Colonel C.R. Gow) of Gow Construciton Co. in Boston began making exploratory boring using 1-inch diameter drive samplers. After modifications by Harry Mohr to the initial test by Gow, it was first called the "Standard Penetration Test" in 1947 in a presentation by Karl Terzaghi. The SPT as in 1947, was defined as the number of blow counts per foot of penetration on a 18-inch deep sample round, using a 140-lb hammer dropping 30 inches, pushing a 2-inch outside diameter sampler (fig. 3.3). However the standardization of the test failed and engineers used whatever devices they had previously, and therefore correlation equations were derived. The SPT blowcount by Mohr is now referred to as N_{60} because Mohr's hammer was lifted by a rope wrapped around

a rotating drum and let free, which is not as efficient as an ideal triggering device giving a truly free fall which was considered as 100% efficient. After refinements of initial correlation relationships, the standard blowcount is defined today as:

$$(N_1)_{60} = (N)_{60} C_N \tag{3.7}$$

where N_{60} is the standard penetration test (SPT) value, corrected for field procedures and apparatus, $(N_1)_{60}$ is the SPT value normalized to an equivalent σ'_{v0} of one atmosphere, and C_N is the overburden correction factor. Amongst others (Liao and Whitman [64], Boulanger and Idriss [11]), Boulanger [10] proposed the following expression to derive C_N:

$$C_N = (\frac{P_a}{\sigma'_{v0}})^m \tag{3.8a}$$

$$m = 0.784 - 0.521 D_R \tag{3.8b}$$

where D_R is the relative density of the soil which is a function of the *in situ* void ratio (e) and the minimum and maximum practical values ($D_R = (e_{max} - e)/(e_{max} - e_{min})$).

The SPT blowcount calculated by eq. 3.7 provides an estimate of the cyclic shear strength of the soil, which is the cyclic stress ratio which is required to cause initial liquefaction of the soil in the specified number of cycles. To estimate the cyclic stress ratio (CSR) of a certain earthquake scenario, a simplified procedure was proposed by Seed and Idriss [103] using the following expression:

$$CSR = \frac{(\tau_h)_{ave}}{\sigma'_0} = 0.65 \frac{\alpha_{max}}{g} \frac{\sigma_0}{\sigma'_0} r_d \tag{3.9}$$

where σ_0 is the total overburden pressure on sand layer under consolidation (it is presumed that for marine sediments it should be only the saturated soil column and not the whole water column to the sea surface [92]); σ'_0 is the initial effective overburden pressure of the sand layer under consolidation; α_{max} is the maximum ground acceleration induced by the earthquake; and r_d is the stress reduction factor varying from a value of 1 at the ground surface to a value of 0.9 at a depth of about 9.6m. The stress reduction factor is used to describe the true behavior of a flexible soil column under earthquake loading, where cyclic stresses do not vary linearly with depth as they would do for a rigid soil column (figure 3.4). It can be calculated by the following relation (Idriss [51]):

If $z \leq 34m$

$$ln(r_d) = \alpha(z) + \beta(z) M_w \tag{3.10a}$$

$$\alpha(z) = -1.012 - 1.126 sin(\frac{z}{11.73} + 5.133) \tag{3.10b}$$

$$\beta(z) = 0.106 + 0.118 sin(\frac{z}{11.28} + 5.142) \tag{3.10c}$$

If $z > 34m$

$$r_d = 0.12 exp(0.22 M_w) \tag{3.10d}$$

where z is in meters and M_w is the moment magnitude. The uncertainty in r_d increases with increasing depth and eq. 4.8 should be applied for depths less than about 20m (Idriss and Boulanger [52]).

It is customary to adjust the CSR value to the equivalent of a magnitude $M_w = 7.5$ earthquake by introducing the magnitude scaling factor (MSF):

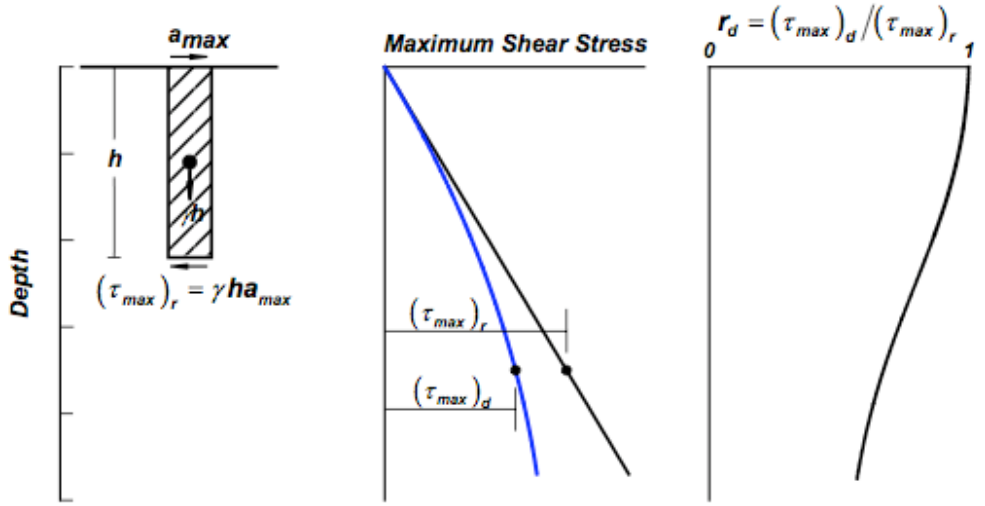

Figure 3.4: Schematic for determining maximum shear stress (τ_{max}) and the stress reduction coefficient (r_d) (after Seed and Idriss [103])

$$(CSR)_{7.5} = \frac{CSR}{MSF} = 0.65 \frac{\alpha_{max}}{g} \frac{\sigma_0}{\sigma'_0} \frac{r_d}{MSF} \tag{3.11}$$

where MSF is the magnitude scaling factor which provides an approximated representation of the effects of shaking duration or equivalent numbers of stress cycles (Idriss and Boulanger [52]). Idriss [51] derived a relation for MSF as:

$$MSF = 6.9 exp(\frac{-M}{4}) - 0.058 \tag{3.12a}$$

$$MSF \leq 1.8 \tag{3.12b}$$

Following earthquakes, engineers studied the areas where liquefaction had and had not occurred and developed criteria, based primarily on the standard penetration resistance of the sand deposits, for differentiating between liquefiable and nonliquefiable conditions. A comprehensive collection of site conditions at various locations led to production of charts such as that shown in fig. 3.5 to allow for evaluation of liquefaction potential for different magnitude earthquakes. By plotting a point corresponding to the blow count for the site and to the design earthquake ground motion it can be determined whether the site is susceptible to liquefaction or not. If the point plots below the curve the site is judged to be safe and if it plots above the curve it is considered susceptible to liquefaction. The cyclic resistance ratio is obtained from the appropriate curve in the figure for the corresponding $((N_1)_{60}$ and moment magnitude values. Then, by comparing the cyclic resistance ratio (CRR) to the cyclic stress ratio (CSR) the factor of safety can be expressed as:

$$F_s = \frac{CRR}{CSR} \tag{3.13}$$

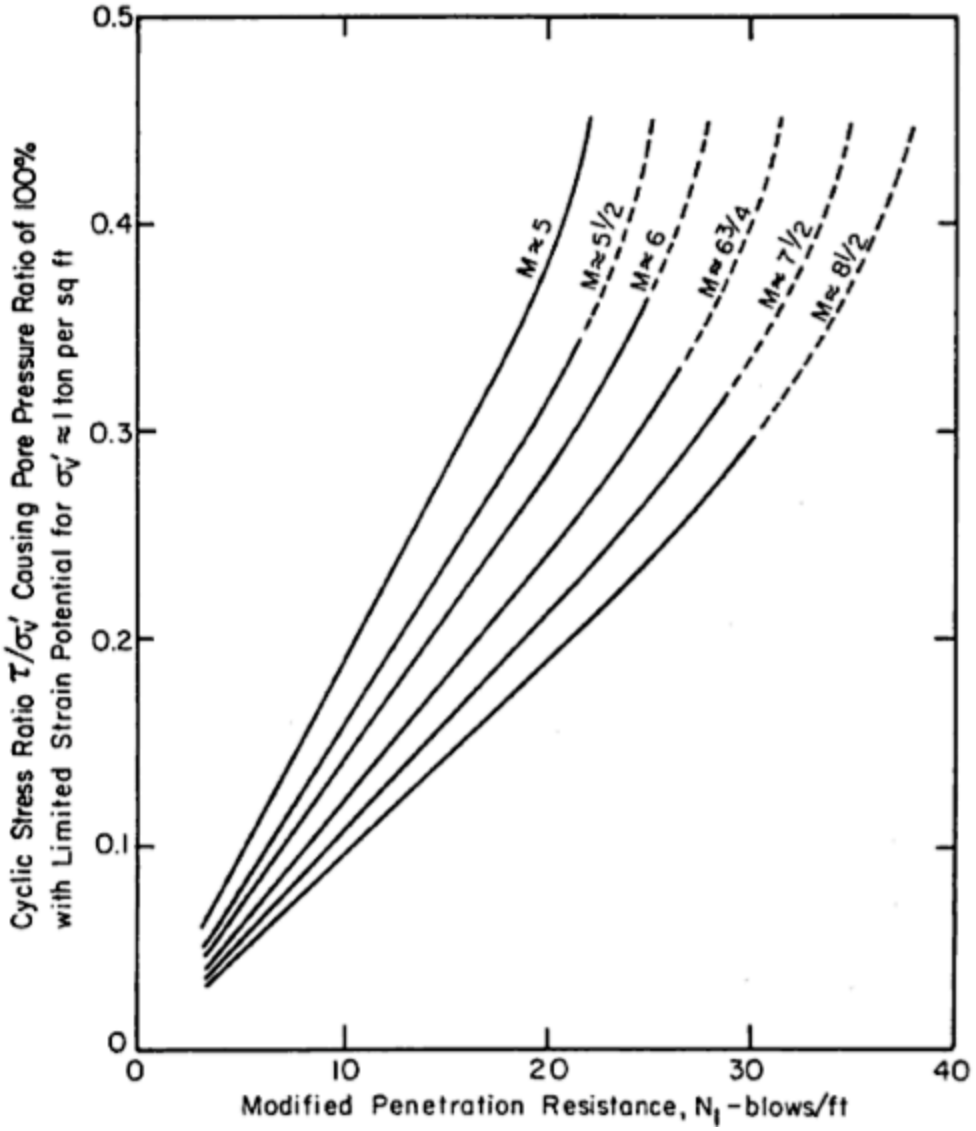

Figure 3.5: Chart for evaluaiton of liquefaction potential of sands for earthquakes of different magnitudes (Seed and Idriss [106])

Table 3.3: Effective stress strength parameters of calcareous soils (after Poulos [92]).

Reference	Soil type	Carbonate content (%)	Location	Test type	Confining pressure of vertical stress (kPa)	c' (kPa)	$\phi'(^o)$	Remarks
Nacci *et al.* (1974)	silicious calcilutite	20.65	Labrador Basin	CIU		2-7	31-37	Cemented samples; confining pressures slightly greater than effective overburden pressure
Nacci *et al.* (1974)	bioclastic carbonate sand	> 85	three from west coast of India; one from islands in Arabian Sea	CID	100	0	49.5-51.0	Similar values for all four soils; c', ϕ' depend on confining stress
				CID	15000	3-9	29-30	
				CID	100	0	42-44.5	and crushing; c', ϕ'
				CID	6400	0	40.5-42	values for peak stress ratio
Poulos *et al.* (1982)	carbonate sand	88	Bass Strait, Australia	CID	138-897	0	46.3-40.4	ϕ' decreased with increasing confining pressure
Demars *et al.* (1976)	various	various	various	CIU	7-70	0-1	27.7-31.3	Effect of carbonate content examined

Chapter 4

Submarine Landslides

4.1 Terminology

Terms provided here are adapted from the Multilingual Landslide Glossary [139] established by the UNESCO Working Party on World Landslide Inventory (WP/WLI) in 1993. Numbers in the list of terms that follows, correspond to the numbers indicated in figure 4.1.

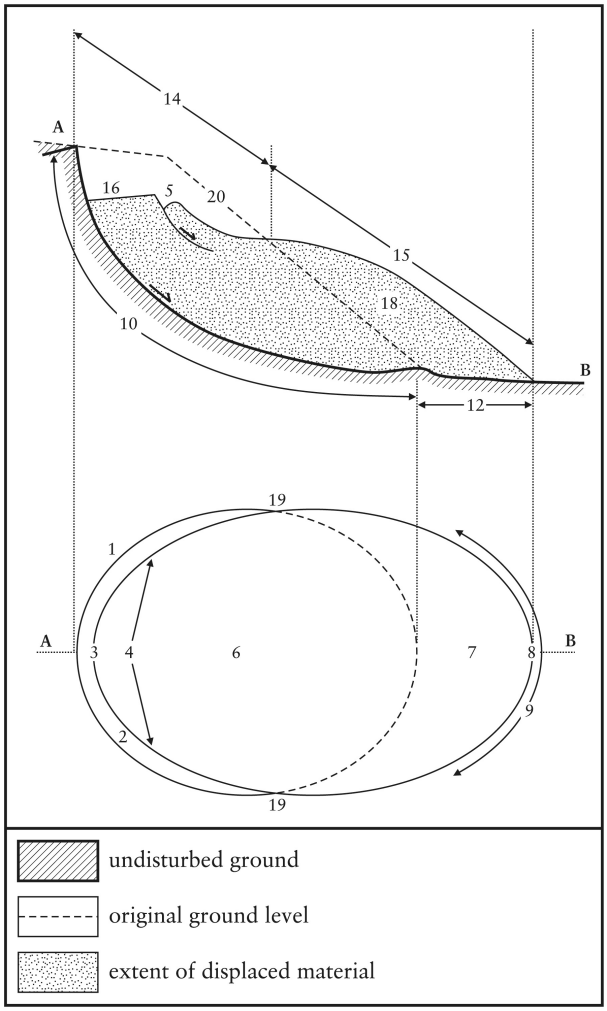

Figure 4.1: Landslide terminology, cross-section and top view (image source Cooper [14]).

[**a**] **Crown:** The practically undisplaced material still in place and adjacent to the highest parts of the main scarp.

[**b**] **Main Scarp:** A steep surface on the undisturbed ground at the upper edge of the landslide, caused by movement of the displaced material away from the undisturbed ground. It is the visible part if the surface of rupture.

[**c**] **Top:** The highest point of contact between the displaced material and the main scarp.

[**d**] **Head:** The upper parts of the landslide along the contact between the displaced material and the main scarp.

[**e**] **Minor Scarp:** A steep surface on the displaced material of the landslide produced by differential movements within the displaced material.

[**f**] **Main Body:** The part of the displaced material of the landslide that overlies the surface of rupture between the main scarp and the toe of the surface of rupture.

[**g**] **Foot:** The portion of the landslide that has moved beyond the toe of the surface of rupture and overlies the original ground surface.

[**h**] **Tip:** The point of the toe farthest from the top of the landslide.

[**i**] **Toe:** The lower, usually curved margin of the displaced material of a landslide, it is the most distant from the main scarp.

[**j**] **Surface of Rupture:** The surface which forms (or which has formed) the lower boundary of the displaced material below the original ground surface.

[**k**] **Toe of the Surface of Rupture:** The intersection (usually buried) between the lower part of the surface of rupture of a landslide and the original ground surface.

[**l**] **Surface of Separation:** The part of the original ground surface overlain by the foot of the landslide.

[**m**] **Displaced Material:** Material displaced from its original position on the slope by movement in the landslide. It forms both the depleted mass and the accumulation.

[**n**] **Zone of Depletion:** The area of the landslide within which the displaced material lies below the original ground surface.

[**o**] **Zone of Accumulation:** The area of the landslide within which the displaced material lies above the original ground surface.

[**p**] **Depletion:** The volume bounded by the main scarp, the depleted mass and the original ground surface.

[**q**] **Depleted Mass:** The volume of the displaced material, which overlies the rupture surface but underlies the original ground surface.

[**r**] **Accumulation:** The volume of the displaced material, which lies above the original ground surface.

[s] **Flank:** The undisplaced material adjacent to the sides of the rupture surface. Compass directions are preferable in describing the flanks but if left and right are used, they refer to the flanks as viewed from the crown.

[t] **Original Ground Surface:** The surface of the slope that existed before the landslide took place.

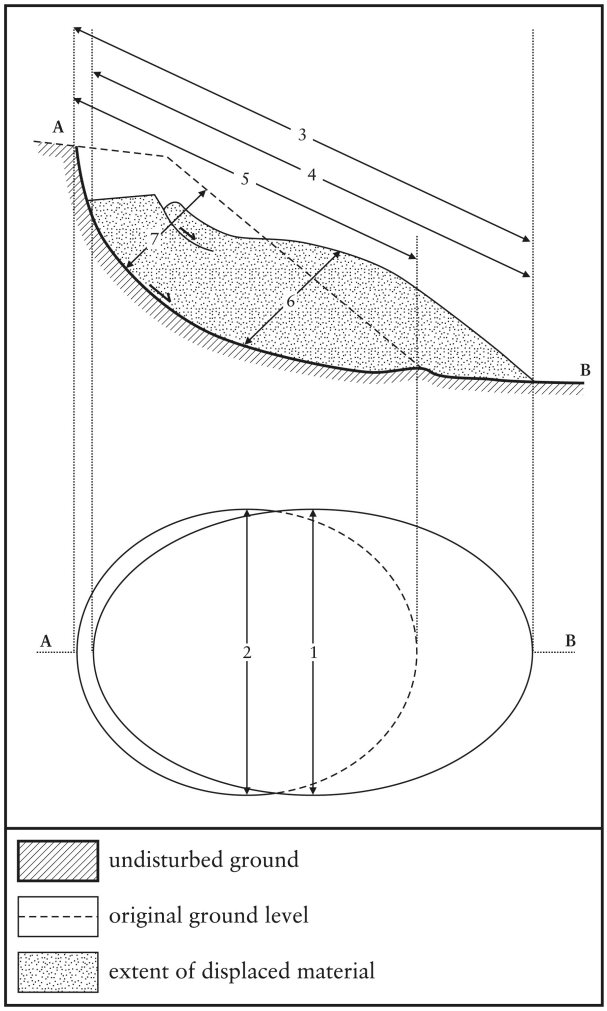

Figure 4.2: Landslide dimensions, cross-seciton and top view (image source Cooper [14])

Landslide dimensions recommended in the Multilingual Landslide Glossary [139] (numbering corresponds to figure 4.2):

[a] **Width of the Displaced Mass:** The width of the displaced mass, W_d, is the maximum breadth of the displaced mass perpendicular to the length of the displaced mass, L_d.

[b] **Width of the Rupture Surface:** The width of the rupture surface, W_r, is the maximum width between the flanks of the landslide, perpendicular to the length of the rupture surface, L_r.

[c] **Total length:** The total length, L, is the minimum from the tip of the landslide to the crown.

[d] **Length of the Displaced Mass:** The length of the displaced mass, L_d, is the minimum distance from the tip to the top.

[e] **Length of the Rupture Surface:** The length of the rupture surface, L_r, is the mimmum distance from the toe of the surface of rupture to the crown.

[f] **Depth of the Displaced Mass:** the depth of the displaced mass, D_d, is the maximum depth of the displaced mass, measured perpendicular to the plane containing W_d and L_d.

[g] **Depth of the Rupture Surface:** The depth of the rupture surface, D_r, is the maximum depth of the rupture surface below the original ground surface measured perpendicular to the plane containing W_r and L_r.

4.2 Types of submarine mass movements

They can all be called "landslides" in a general sense, but the reader should be aware of the different terms used to describe the different forms of slope failure [45], [73]. Here, the term "submarine landslide" is used to include all types of slope failures, but distinction is given in certain parts where it is of special importance. To describe all types of slope failures (mass movements) for submarine landslides, the classification proposed for sub-aerial mass movements by ISSMGE (International Society for Soil Mechanics and Geotechnical Engineering) Technical Committee on Landslides was adopted and adjusted to the marine environment (figure 4.3) by Locat and Lee [69], the only addition being turbidity currents that develop from mobile types of mass movements such as avalanches, debris and mud flows. Mulder and Cochonat [80] propose a different classification for submarine landslides, with three main types of processes of mass movement of which 13 main varieties have been recognized by the authors. Also Moore [78] has proposed a classification of submarine landslides into three general classes, related to the time of their occurrence and the geological processes which caused them [92]. Here the classification proposed by Locat and Lee [69] is adopted which can cover most of the observed phenomena [69]. Each type of mass movement is defined as:

- **Slide:** Is defined as the movement of a coherent mass of sediment bounded by distinct failure plains [73]. It can be divided in rotational and translational slides, depending on the shape of the rupture surface. Rotational slides move along a rupture surface that is curved or concave-upward, are also formally termed as "slumps". In translational slides the mass displaces along a planar rupture surface, sliding over the original ground surface [16].

- **Topples:** Describes the forward or outward rotation of the slope of mass of soil or rock [16]. Following the detachment/rotation, the mass can either fall or slide downslope.

- **Spreads:** This term is used to describe the lateral movement of a coherent layer overtopping a weaker layer that fails as a result of liquefaction or plastic flow [62].

- **Falls:** Usually triggered by earthquake shock, it involves the detachment of masses such as rocks and boulders, occurring in steep slopes, which once detached they either bounce or roll on the seafloor and fall further downslope or just fall until rest. Rock falls and rock avalanches are differentiated by volume of material and duration of the event, the later being more rapid, large-scale catastrophic event [80]. Such type of mass movement can occur in volcanic islands, fjords and submarine canyons [80], [143].

- **Flows:** They usually occur on the continental slope from failure of typically underconsolidated masses of sediment [80]. This type of landslide includes all types of mass movement that resemble that of a viscous fluid:
  - **Debris flow:** involve a matrix, consisting of nonliquefiable and cohesive material which is usually dominated by silt and clay and can support many clasts of consolidated clay [80].
  - **Mud flow:** this type of flow contains more fines and as a result the main parameters controlling the onset of the motion are the yield resistance of the flow and its viscosity whereas in debris flows, gravity is the most important factor [80].
  - **Turbidity current:** gravity flow in which sediment grains are maintained in suspension by fluid turbulence [73]. This is the only mass movement type that occurs exclusively in the marine environment and is very poorly understood process [73].
  - **Debris avalanche:** rapid flow of cohesionless rock fragments with energy dissipation by grain contact [73].

All the above types of mass movement are mutually exclusive, meaning that all have distinct characteristics that allows us to differentiate them from one another. However, a certain mass movement can transform into another during the descent, as for example a slide can transform into a debris flow and then into turbidity current.

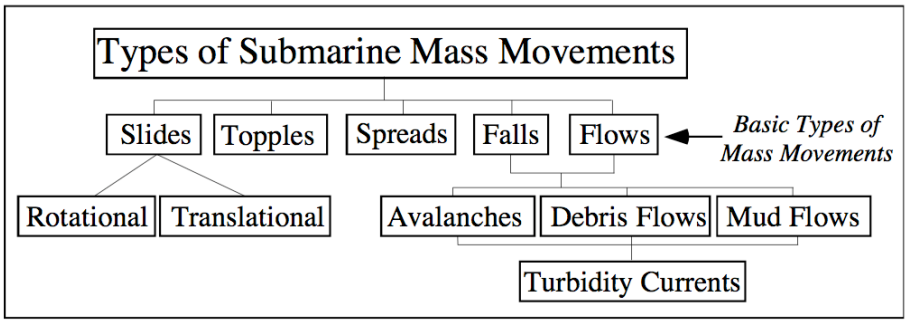

Figure 4.3: Classification of submarine mass movements adapted from sub-aerial classification proposed by the ISSMGE Technical Committee on Landslides (TC-11). [69]

4.3 Triggers

Landslide triggers vary from short lasting processes such as earthquakes, to long lasting processes such as climate change. Usually, slope failure is the result of both long term processes slowly contributing to slope failure and the short-lasting events acting as the final push that triggers the landslide (e.g. a slope may not fail by earthquake loading rapid sedimentation was not present). Masson *et al.* [73] propose, the triggers being divided to those related to geological characteristics of the landslide material (e.g. over-pressure due to rapid deposition or the presence of a weak layer) and those driven by transient external events (e.g. earthquakes or climate change). Geological characteristics can be linked to the transient external events making things even more complicated. For example, the distribution of weak layers, is controlled by regional changes in sedimentation style, which, on an even broader scale, are driven by climate change between glacial and interglacial conditions (Bryn *et al.* (2005) referred in Masson *et al.* [73]).

Hance [46] has created a submarine landslide database, from data available in literature, to determine the important characteristics of failure initiation. He examined statistically, factors such as geographic location, data of failure, soil type, triggering mechanism, slide runout distance, slide size characteristics and water depth of slide initiation. In terms of triggering mechanism causing slope failure (which does not mean that other factors have not contributed as mentioned earlier), information was available for 366 of the 534 landslides in his database. The distribution of triggering mechanisms is shown in figure 4.4. Over 40% of the slides were reported to be triggered by earthquakes. However, often multiple triggering mechanisms were reported rather than a single, because the trigger was uncertain. To be precise, in 86% of the earthquake triggered events the trigger was inferred and only 14% was known. If one plots only the 57 cases for which the trigger is known, magma volcanic activity is the second most frequent reported trigger (fig. 4.5).

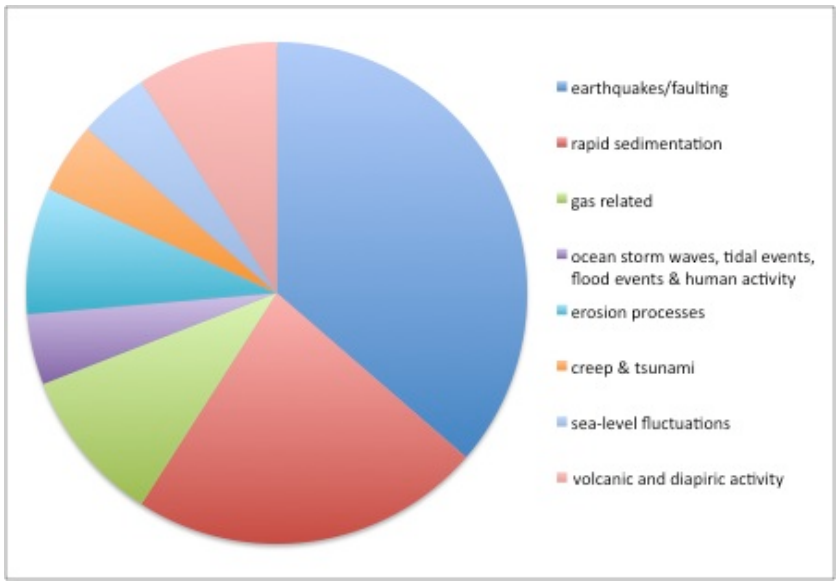

Figure 4.4: Inferred & known triggering mechanisms of submarine landslides reported in literature (data is taken from Hance [46])

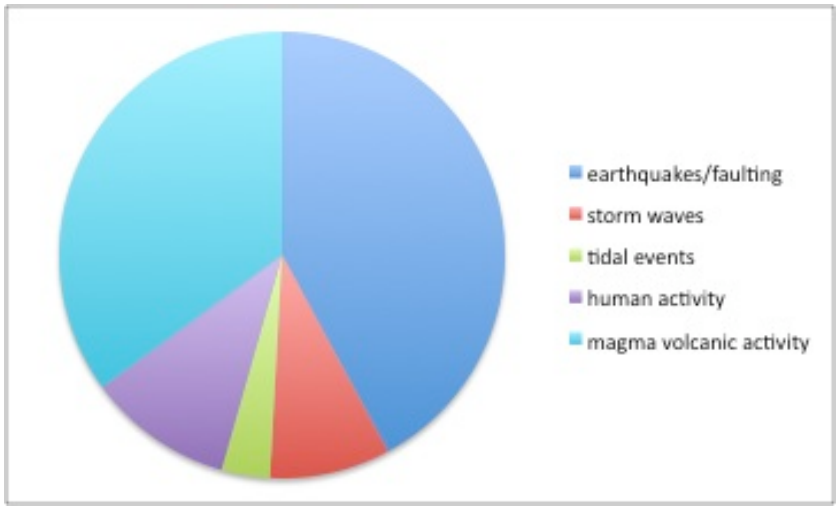

Figure 4.5: Known triggering mechanisms of submarine landslides reported in literature (data is taken from Hance [46])

In this thesis only gravity loads, wave loads, earthquakes and gas hydrates are described and subsequently included in slope stability analysis in chapter 5.

4.3.1 Gravity loads

Actions of gravity loads include (a) the downslope driving forces that initiate slope failures (b) the weight that allows consolidation of sediments and (c) differential stressing due to rapid deposition of dense materials on less dense soils that may produce squeezing and diapirism as material flows plastically from beneath loaded areas [92]. Sedimentation processes can lead to slope failures when the stresses on the seafloor equal or exceed the shear strength. High deposition rates can lead to excess pore water pressures that reduce the shear strength of the soil thus increases the probability of failure. Slope failures under gravity loading can be either rapid or in the form of creep where strains accumulate over time and under high stress ratios can result in failure.

4.3.2 Earthquakes and tectonic activity

Earthquakes are the result of sudden release of stress accumulated over time along planes of weakness such as geologic faults. Once the stresses exceed the shear strength of the faulted rock (rigidity) fault rupture is initiated, stresses are transferred to nearby points and rupture propagates along the fault. In big earthquake events, aftershocks will follow until stresses are released. The extend of rupture propagation will determine the magnitude of the earthquake and the amount of energy released (see section 6.2).

Earthquakes radiate energy in the form of seismic waves that can be detected thousands of kilometers away from the epicenter through sensitive seismographs. Seismic waves are divided in body waves and surface waves. The former include the P, Primary (longitudinal or compressional) waves and the S, Secondary (transverse or shear) waves. Surface waves include Rayleigh and Love waves. Body waves are the first to arrive, with the P waves traveling faster and being used for epicentral-hypocentral location and time origin determination. The surface waves are typically the most destructive waves.

To quantify the amount of energy released by an earthquake event many magnitude scales have been proposed, starting with Richter's local magnitude scale M_L in the 1930s. Although reasonably consistent with each other, they are not directly related because they don't measure the same quantities. The most common magnitudes used are the body wave magnitude M_b and the surface wave magnitude M_s. The former measures the highest instrument response of P waves at a period of 1sec and the later measures the highest instrument response of Rayleigh waves at a period of 20sec. However, as the size of the earthquake grows, the source is longer and the energy is released in higher periods. Therefore measuring earthquakes at fixed periods the true size of large events is missed. This is called saturation and is shown in figure 4.6.

The only magnitudes that capture the true size of the earthquake regardless the size of the event are the moment magnitude M_w and the mantle magnitude M_m. The mantle magnitude was introduced by Okal and Talandier [87] uses Rayleigh waves, as is used with the surface magnitude, but with variable period. It is directly related to seismic moment M_0 defined as:

$$M_0 = \mu L W \Delta u \tag{4.1}$$

where μ is earth's rigidity ($\approx 3 \cdot 10^{10} Nm^{-2}$ in the crust or $\approx 7 \cdot 10^{10} Nm^{-2}$ in the mantle), L is the fault rupture length, W is the fault rupture width and Δu is the average fault slip (figure

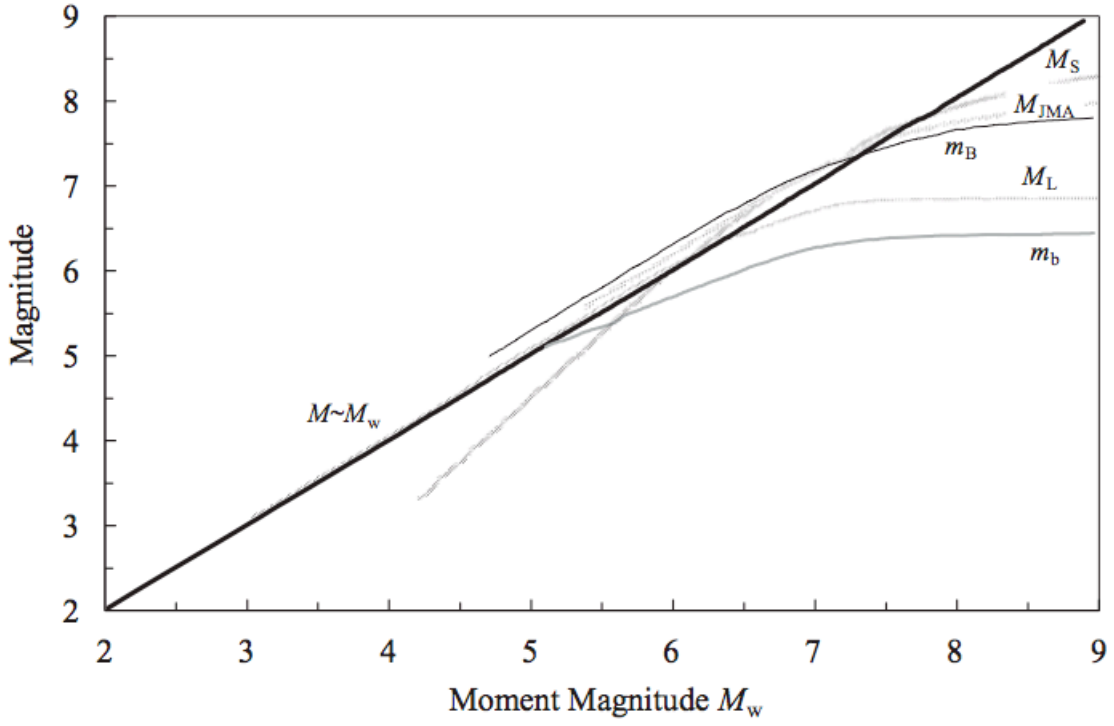

Figure 4.6: Saturation of magnitude scales (after Elnashai and Di Sarno [25])

4.7). The amount of energy released from the earthquake is directly related to seismic moment by (Hanks and Kanamori [47]):

$$E_s = \frac{\Delta\sigma}{2\mu} M_0 \tag{4.2}$$

where $\Delta\sigma$ is the stress drop.

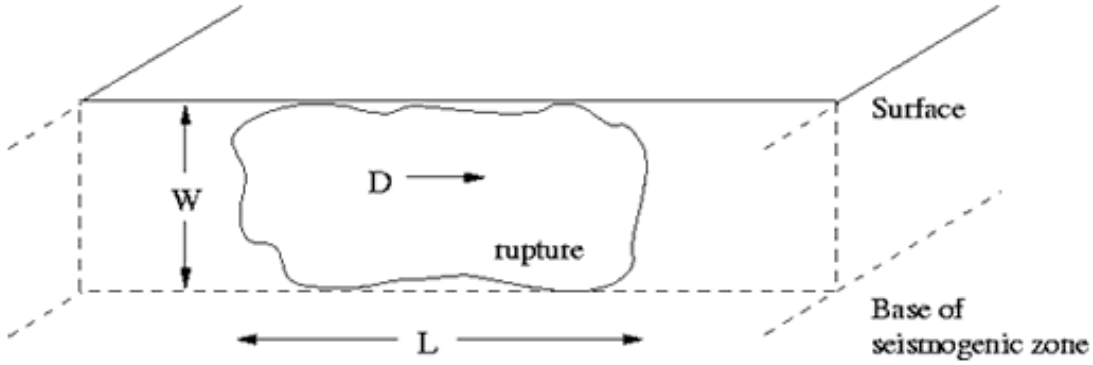

Figure 4.7: Fault rupture area and average slip used to determine seismic moment M_0 [150].

Kanamori [57] and Hanks & Kanamori [47] introduced the moment magnitude given by:
M_0 in Nm

$$M_w = \frac{2}{3} (\log M_0 - 9.1) \tag{4.3a}$$

M_0 in dyne cm

$$M_w = \frac{2}{3} (\log M_0 - 16.1) \tag{4.3b}$$

Equations 4.1 and 4.3 are used to calculate seismic moment and corresponding moment magnitude given the rupture area and slip distribution. Rupture area ($A = LW$) is determined from aftershock distribution or waveform analysis of seismograms produced by an earthquake.

Of engineering interest is the ground motion produced by earthquakes waves, who's intensity is a function of distance from the fault rupture area, the magnitude of the earthquake, depth and local site conditions. The attenuation of earthquake ground motion can be calculated from area-specific empirical relationships that have been derived and have the following form (Elnashai and Sarno [25]):

$$log(Y) = log(b_1) + log[f_1(M)] + log[f_2(R)] + log[f_3(M,R)] + log[f_4(E_i)] + log(\epsilon) \tag{4.4}$$

where Y is the ground motion parameter to be computed, b_1 is a scaling factor. The 2nd to 4th terms are functions of magnitude M, source-to-site distance R, and possible source, site and geologic and geotechnical structure effects E_i (Elnashai and Sarno [25]). ϵ represents the uncertainty and errors involved in the regression analysis to derive the attenuation relationship. Ground motion parameters of interest include Peak Ground Acceleration (PGA), Peak Ground Velocity (PGV), Peak Ground Displacement (PGD), Spectral acceleration (S_a), Spectral velocity (S_v) and Spectral displacement (S_d).

Ground motion determines the forces exerted on ground and through the ground to structures. The earthquake response of the underlying soil and that of the structure is a result of complex interaction between random input ground motion and the continuously changing dynamic characteristics of the soil layers and the overlying structure. In addition, ground motion is exerted in all three dimensions, two horizontal and one vertical making things even more complicated. In order to simplify the slope stability analysis, it is common to assume that only horizontal ground motion contributes to slope failure and an equivalent static load is derived to convert the dynamic problem into static (as shown in fig. 4.8). Consequently, seismic loading is represented by an maximum seismic coefficient k (unit-less, percentage of gravity acceleration) which is a function of input ground motion and the geometry of the sliding mass. The earthquake driving force is then simply determined by multiplying k with the weight of the slice. Sometimes k is assumed as being equal to PGA although that is not true. As explained earlier a dynamic problem is converted to static and therefore peak ground acceleration which is a momentary value in the time domain of input ground motion cannot correspond a static force. But if it is assumed that $k = PGA$ it usually yield conservative results.

As described in section 3.3 cyclic loading due to earthquake can cause pore water pressure rise and potentially lead to loss of effective strength of the soil (liquefaction). Secondary effects of long-term tectonic activity include uplift of sea floor affecting temperature and pressure environment for gas hydrate disassociation [127] (see section 4.3.4) and tsunami generation. The tsunami can cause slope failure due to either the hydrodynamic pressures applied on the seafloor (sections 4.3.3 and 5.4) or due to the rapid drawdown that occurs when a LDN tsunami (see section 6.1) approaches a shoreline that removes the resisting force exerted by the water and induces an undrained loading conditions.

4.3.3 Hydraulic forces

Hydraulic forces on seabed may arise from tides, storm waves, currents or tsunamis. Currents act as a horizontal force on the seabed causing erosion and deposition, which can alter the effective overburden pressure. Tsunamis and tides can usually affect soft sediments in the intertidal zone and immediate adjacent areas where a sudden lowering of water level removes

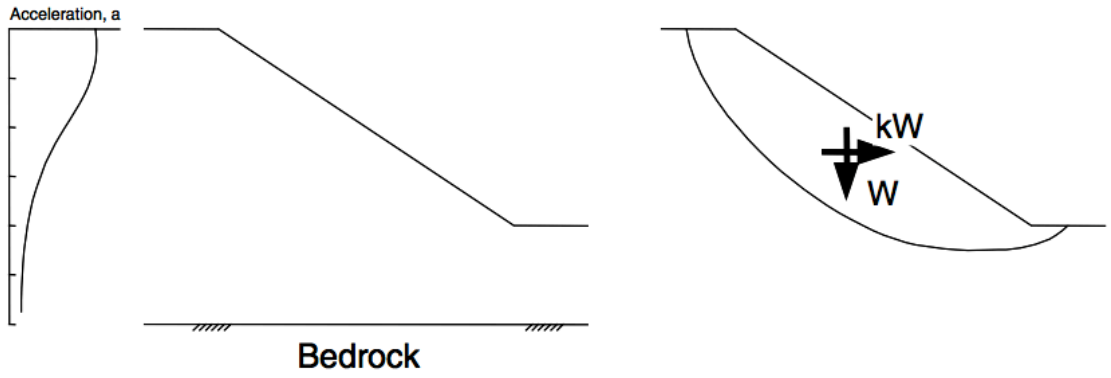

Figure 4.8: Simplified representation of earthquake acceleration used in pseudo-static stability analysis (after Wright and Rathje [140]).

the resisting forces provided by the external waves along the slope. However, tides arising from storm surge associated with cyclone and hurricane action can have an impact at greater depths [92]. Storm waves can generate adjacent zones of relatively high and low pressure on the seabed beneath the crest and trough of the wave respectively that in turn induce cyclic stresses that tend to shear and possibly displace the soil downslope (figure 4.9). As will be seen in section 5.4, bottom pressure decreases with depth and therefore the importance of storm wave induced bottom pressures limited to depths less than 150 to 300m [29], [92]. Other wave types include infra-gravity waves (wave periods in excess of 1min) and internal waves due to temperature or salinity variations. Internal waves have little significance but infra-gravity waves due to their long period (and thus big wave length) can have an impact on slope stability depending on the wave height [92].

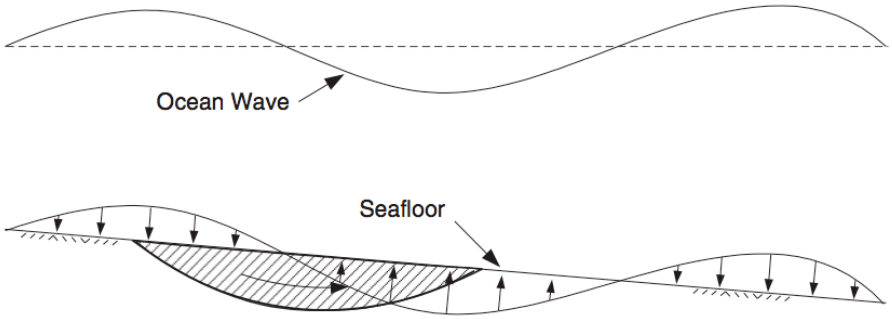

Figure 4.9: Seafloor instability produced by ocean wave-induced hydrodynamic pressures (after Wright and Rathje [140]).

4.3.4 Gas hydrates

Another cause of slope failure is the presence of gas hydrates. Such hydrates are crystalline solids, similar to ice, except that the crystalline structure is stabilized by the guest gas molecule within the cage of water molecules [144]. The most common gas contained in submarine gas hydrates is methane [127]. They form at low temperatures and moderate to high pressure conditions due to the decomposition of biological material in areas of rapid accumulation of detritus and sapid accumulation of sediments (fig. 4.10). Temperature and pressure conditions consistent with methane hydrate stability are found at the seafloor nearly everywhere at water

depths exceeding 300-800m, depending on regional seawater temperature [127]. They may disassociate into natural gas under certain temperature and pressure conditions. The release of gas in the form of bubbles can reduce shear strength and contribute to slope failure as will be shown in slope stability analysis that follows.

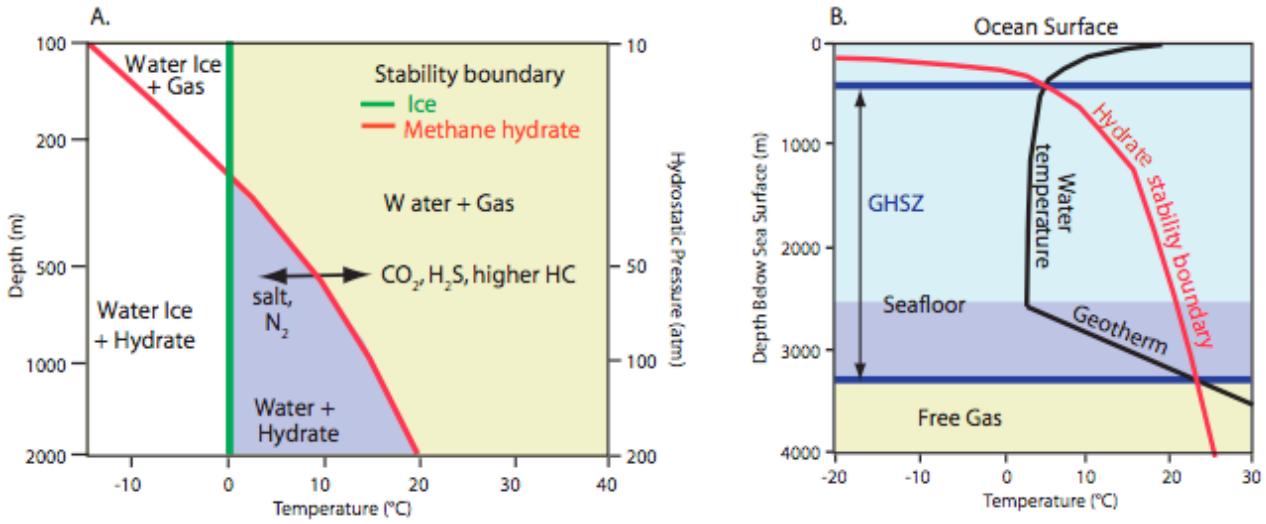

Figure 4.10: The methane hydrate stability boundary compared to water ice stability for fresh water. The stability boundary moves to the right if gas contains CO_2, H_2S, or higher-order hydrocarbons and to the left as pore-water salinity increases or if the gas contains N_2. (B) Gas hydrate stability in the marine environment. The gas hydrate stability zone (GHSZ) extends from the depth within the ocean at which gas hydrate becomes stable (which depends on local water temperature) to a depth beneath the sea oor that is determined by the local geothermal gradient. Much of the sea oor is within the GHSZ. The thickness of the GHSZ below the seafloor increases as water depth increases if the geothermal gradient is constant. (source: Trehu *et al.* [127])

Chapter 5

Slope Stability

5.1 General

Stability of slopes is an important aspect in engineering that has to be incorporated in structural design when slope failure is likely to occur. Calculating the probability of slope failure is not straightforward and needs many parameters to be taken into consideration. In contrast to sub-aerial slides, in the submarine environment slope failures can occur even on very gentle slopes as low as 1 showing that a thorough examination is required to identify areas that are prone to slope failures in order to perform hazard studies. An assessment of stability of the sea floor has to include investigation and interpretation of geological history, stratigraphic structure, sedimentology and morphology of the region as well as identification and evaluation of the topographic profile and deformational features of the sea floor [92]. For the estimation of stresses in the seafloor various loading conditions have to be taken into account that can cause slope failure, which are not necessarily mutually exclusive. Triggering mechanisms can be either direct, such as inertial forces from earthquake shaking, or indirect, such as the hydrodynamic pressures on the seafloor due to a tsunami which was generated by the earthquake. Failure can be initiated either by reduction of the shear strength of the soil which decreases the resisting forces in the slope, or by the increase of the driving forces in the slope or by both. The four most common mechanisms of instability are considered here, namely: gravity forces, earthquakes, hydraulic forces and gas hydrates.

5.2 Slope stability analysis

In slope stability analysis, three approaches exist: *limit equilibrium*, *continuum mechanics* and *finite element* analysis. All commonly assume plain strain for simplification. In *continuum analysis* the shear stresses in the soil at different depths are computed, developed by wave or earthquake loading, and then they are compared to the corresponding shear strength of the soil taking into account effects of cyclic and/or dynamic loading on the shear strength [92]. Failure occurs when the shear stress exceeds the shear strength. *Finite element analysis* is a computational method, where the soil is discretized using finite elements and has the great advantage of being able to handle non-homogeneous or anisotropic soil behavior, automatically detect critical slip surfafes/failure modes and calculate strains and displacements. However, using finite elements, data preparation can be cumbersome and assigning soil parameters is very difficult when accurate information lacks.

In this thesis only the method of limit equilibrium is adopted and more details about this method are given in the following section.

5.2.1 Limit equilibrium methods

Limit equilibrium methods are the most widely used for slope stability analysis. The basic principle in this method is to compare resisting to overturning moments or forces and determine the factor of safety. It is considered that failure is on the point of occurring along an assumed or a known failure surface [13]. In a deterministic analysis, for any given slope, failure occurs when the applied shear stress exceeds the residual shear strength on the potential failure surface. The factor of safety (F) is given by:

$$F = \frac{\text{shear strength}}{\text{shear stress}} \tag{5.1}$$

For factors of safety greater than 1.0 the slope is considered to be stable. In probabilistic analysis uncertainties in the loading and shear strength of the sediments is accounted for and the outcome of such an analysis is a relationship between probability of failure and the width and depth of the failure surface [92]. Here, only deterministic analysis is performed.

In section 4.2 various types of submarine landslides were described according to international classification. Limit equilibrium methods, in a more general sense, may involve circular or non-circular failure surfaces depending on the type of slope failure expected. *Rotational* slip failure surfaces may be either circular or non-circular depending on homogeneity of soil conditions [13]. *Translational* and *compound* slips occur in the presence of adjacent stratum of significantly different strength. In the case of *translational* slip, the adjacent stratum is at relatively shallow depth below the surface of the slope and therefore the failure surface tends to be plane and roughly parallel to the slope [13]. In the case of submarine slopes, which are gentle and extensive, many seafloor slides involve large distances laterally in comparison to the thickness of the slide mass failure, and it can be assumed that failure occurs on a plane or planes parallel to the surface. Therefore only the *translational* slip type of slope failure is analyzed here using the *infinite slope* method.

Stability analysis methods for circular failure surfaces include:

[**I**] Method of slices

(a) Fellenius ordinary method
(b) Bishop (1955) simplified method
(c) Spencer (1967)
(d) Morgenstern and Price (1965)
(e) GLE

[**II**] Chart solutions based on method of slices

(a) Taylor (1937)
(b) Bishop and Morgenstern (1960)

more on these methods can be found in Craig (1997).

In the following sections slope stability analyses assuming an infinite slope is presented for the various loading conditions present in the submarine environment, namely: gravity loading, wave action, earthquake loading, sedimentation, seepage and gas generation.

5.3 Slope stability under gravity forces

Slope stability analysis under gravity loading can be performed for (i) the undrained condition, relevant to cases of rapid deposition or erosion, earthquake and ocean wave loading as well as gas hydrate disassociation (ii) fully drained, in which no excess pore water pressure exists and (iii) partially drained, in which pore water pressure dissipation has occurred but excess pore water pressure still exists, as in the case of gas generation and sedimentation. Figure 5.1 shows the equilibrium of forces for any vertical slice of a slope for all three conditions.

5.3.1 Undrained conditions

Undrained conditions apply in cases where rapid loading does not allow for drainage and therefore dissipation of pore water pressure. Such loading can be earthquake loading, wave loading, gas hydrate disassociation, rapid deposition or erosion as mentioned earlier. The shear strength of the soil (s_u) in terms of total stresses, is determined by the cohesion intercept $s_u = c_u$ since the friction angle *(ϕ)* is zero.

Equilibrium of forces along the failure plane resolves to:

$$c_u l = W' \sin\alpha \tag{5.2}$$

where W' is the effective weight of the slice, l is the length of the slide along the base and α is the slope angle.

Eq. 5.2 can be rewritten as:

$$\sin 2\alpha = 2c_u/\sigma'_{v0} \tag{5.3}$$

The factor of safety being equal to:

$$F = \frac{2}{\sin 2\alpha}\ (\frac{c_u}{\sigma'_{v0}}\ ) \tag{5.4}$$

5.3.2 Fully drained conditions

In fully drained conditions, no excess pore water pressure exists and hence it is not considered in the analysis.

Equilibrium of forces along the failure plane resolves to:

$$(c' + \sigma' \tan\phi')l = W' \sin\alpha \tag{5.5}$$

Substituting σ' and W':

$$(c' + \sigma'_{v0} \cos^2(\alpha) \tan(\phi'))l = \sigma'_{v0} l \sin(\alpha) \tag{5.6}$$

Rearranging and substituting the overburdern pressure σ'_{v0} with $\gamma' h$ leads to:

$$\tan\alpha = \tan\phi' + \frac{c'}{\gamma' h}\ \sec^2\alpha \tag{5.7}$$

For normally consolidated and under-consolidated sediments in which c' is zero, maximum slope angle is equal to the effective angle of friction (ϕ'). *(ϕ')* is usually higher than 20^o [74] and therefore slope failure under gravity loading alone, in drained conditions is unlikely to occur in

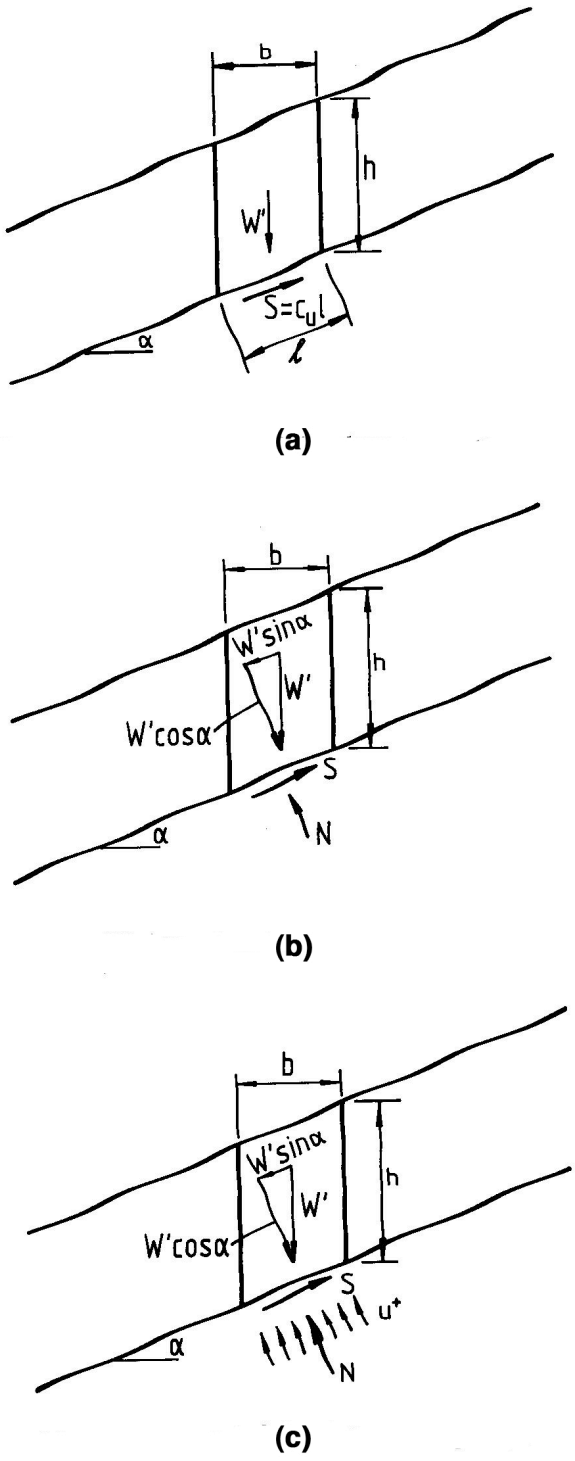

Figure 5.1: Equilibrium of an infinite slope; (a) Undrained conditions (b) drained conditions (c) partially drained conditions (Poulos [92]).

the generally gentle slopes of the marine environment. This can only be possible in slopes that have already failed and moved substantially, thus reducing the drained friction angle along the sliding zone to the residual value that can be less than 10^o in some cases [92].

5.3.3 Partially drained conditions

Partially drained conditions commonly apply to areas of rapid sedimentation, like river deltas, where rapid deposition tends to generate excess pore water pressures in mostly under-consolidated soils.

Pore water pressure in this case is not fully dissipated through drainage and therefore is included in calculation of slope stability. Equilibrium of forces along the failure plane resolves to:

$$(c' + \sigma' \tan \phi')l = W' \sin \alpha \tag{5.8}$$

Substituting σ' and W':

$$(c' + (\sigma'_{v0} \cos^2(\alpha) - u^+) \tan(\phi'))l = \sigma'_{v0} \cos(\alpha) l \sin(\alpha) \tag{5.9}$$

where u^+ is the excess pore water pressure.

Rearranging and substituting the overburdern pressure σ'_{v0} with $\gamma' h$ leads to a safety factor of:

$$F = \frac{c' + (\gamma' h \cos^2 \alpha - u^+) \tan \phi'}{\gamma' h \cos \alpha \sin \alpha} \tag{5.10}$$

Since for under-consolidated sediments c' is zero, the maximum slope angle is given by:

$$\tan \alpha = \tan \alpha (1 - \frac{u^+}{\gamma' h} \sec^2 \alpha) \tag{5.11}$$

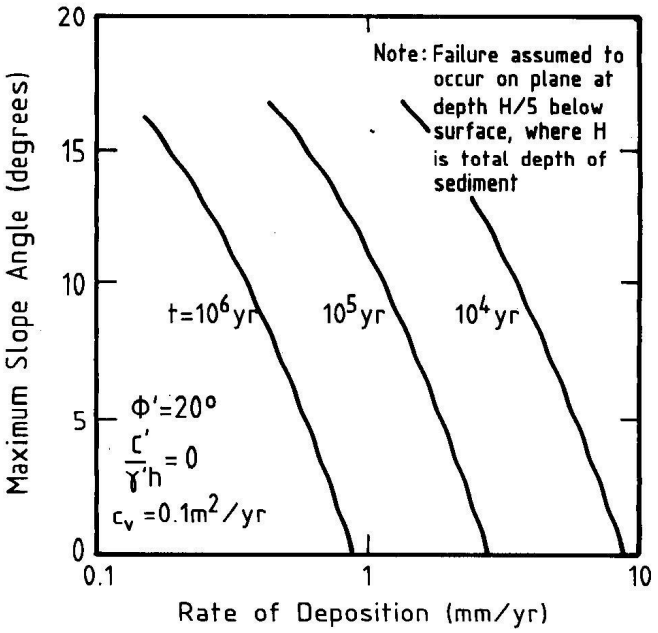

Figure 5.2: The influence of rate of deposition and time on maximum slope angle. (Poulos [92]).

Figure 5.2 shows the maximum slope angle as a function of the rate of deposition for three periods of continuous deposition; 100, 1000 and 10000 years (coefficient of consolidation is taken as $0.1 m^2/yr$). From the figure it can be seen that gentle slopes can only fail from high

deposition rates for a very long period of time. For normal deposition rates of the order of 0.1 mm/year [74] and according to the figure there it is unlikely that failure can be initiated from rapid sedimentation. However with lower consolidation coefficients of the order of 10-5 m^2/yr, associated with impermeable soils, failure could be initiated with a slope angle of 5^o after a million years in a deposition rate of 0.006 mm/yr [92].

5.4 Gas hydrates

In the case of gas hydrates the same conditions apply as in the partially drained case presented in the previous section, where an excess pore water pressure exists reducing the effective strength of the sediment. In this case the excess pore water pressure is a result of gas hydrate dissociation, i.e. the solid hydrate becoming liquid water and gas (usually methane). This results in the formation of a weak layer prone to failure.

Grozic and Kvalstad [41], assuming the water is incompressible and the compression of the gas phase to follow Bolyes law, proposed a simple model to determine the excess pore water pressure due to gas hydrate dissociation. First it is checked whether gas hydrates could exist under the given conditions by:

$$lnP = 38.98 - \frac{8533.8}{T + 273.15} \tag{5.12}$$

where P is the pressure in kPa and T is the temperature in ^0C (for $T \geq 0^0C$). If the conditions are within the gas hydrate stability zone, excess pore water pressure is calculated by:

$$\Delta\sigma' = -\Delta u = u^+ = M[n(1 - S_r)(0.13 - 164.6\frac{T_{eq}}{298.15}\ \frac{1atm}{P_{eq}})] \tag{5.13}$$

where T_{eq} is the equilibrium temperature of gas hydrate in Kelvin, P_{eq} is the equilibrium pressure of gas hydrate in atm, $\Delta\sigma'$ is the change in effective stress caused by melting of gas hydrate, n is the porosity, S_r is the degree of water saturation (eq. 2.8), Δu is the change in pore pressure, and M is the confined compression modulus of soil. This equation is based on each volume of hydrate producing 164.6 volumes of methane gas and 0.87 volumes of water at standard pressure temperature conditions. The confined compression modulus of the soil is given by:

$$M = \frac{(1 + e)\sigma'}{0.434C_s} \tag{5.14}$$

where e is the porosity (see section 2.1.1), and C_s is the the swelling index which can be approximated by (Wroth [141]):

$$C_s = \frac{PI \cdot G_s}{200} \tag{5.15}$$

where PI is the plasticity index and G_s is the specific gravity (see section 2.1.1).

Once the excess pore water pressure is calculated from eq. 5.12, the factor of safety can be calculated from eq. 5.10.

5.5 Slope stability under wave loading

In the simplest form, linear wave theory can be utilized using Airy waves, to estimate wave-induced bottom pressures, assuming that the amplitude of the wave is small with respect to

the depth and the waves have small water surface angles. Velocity potential, water surface elevation and wavelength are given by:

$$\Phi(x,z,t) = \frac{gH}{2\omega}\ \frac{\cosh(\lambda(z+h))}{\cosh(\lambda h)}\ \sin(\lambda x - \omega t) \tag{5.16a}$$

$$\eta(x,t) = \frac{H}{2}\ \cos(\lambda x - \omega t) \tag{5.16b}$$

$$L = \frac{gT^2}{2\pi}\ \tanh(\lambda h) \tag{5.16c}$$

where t is time, x is the horizontal coordinate relative to the node of the wave, $\lambda = 2\pi/L$ is the wave number, $\omega = 2\pi/T$ is the angular frequency, T is period, L is the wavelength, z is the depth from the water surface, h is the depth to the seafloor and H is the wave amplitude as shown in figure 5.4. By plotting the hyperbolic tangent figure 5.3 the relative depths can be identified: shallow, intermediate and deep water.

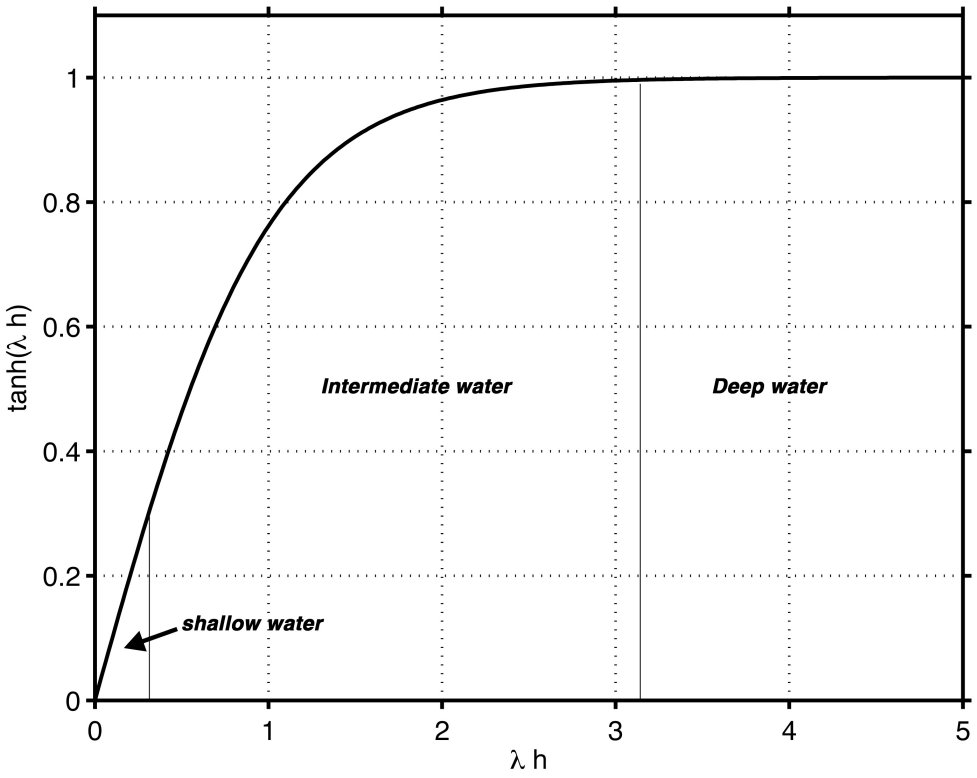

Figure 5.3: Relative depth and asymptote of hyperbolic tangent.

Shallow water

Shallow water lies on the linear part ($\lambda h < \pi/10$) of the hyperbolic tangent function and by approximating $\tanh(\lambda h) \approx \lambda h$ the wavelength in eq. 5.16c and wave celerity $c = L/T$ equal to:

$$L^2 = gT^2 h \tag{5.17a}$$

$$c = \sqrt{gh} \tag{5.17b}$$

Deep water

Deep water starts where the hyperbolic tangent reaches an asymptote at $\lambda h \approx \pi$ Wavelength and celerity are given by:

$$L = \frac{gT^2}{2\pi} \tag{5.18a}$$

$$c = \frac{gT}{2\pi} \tag{5.18b}$$

5.5.1 Wave-induced bottom pressure

The pressure profile due to ocean waves is given by the hydrodynamic component of pressure as:

$$p = \frac{\rho g H}{2} \frac{\cosh \lambda(z+h)}{\cosh \lambda h} \cosh(\lambda x - \omega t) \tag{5.19}$$

At the bottom (z = -h) the pressure becomes:

$$p = p_0 \cos(\lambda x - \omega t) \tag{5.20}$$

where p_0 is the pressure amplitude defined as:

$$p_0 = \frac{\rho g H}{2} \frac{1}{\cosh(\lambda h)} \tag{5.21}$$

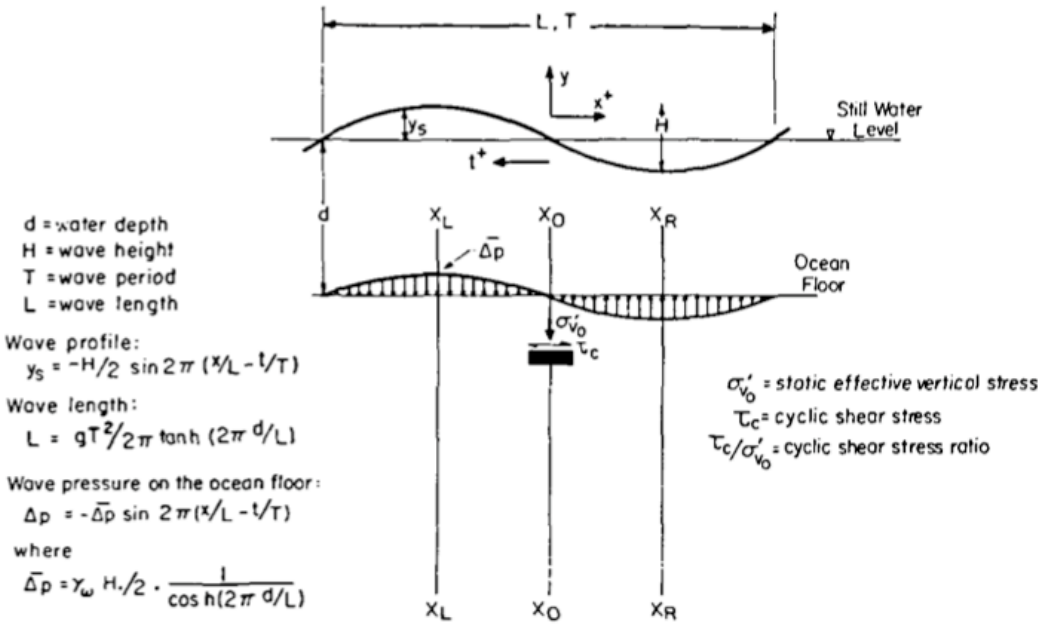

Figure 5.4: Wave characteristics and mechanism of pore-pressure generation (after Suhayda [112]).

Suhayda [112] stresses that field measurements have shown that wind-wave induced pressures can be much higher than predicted by linear theory as much as three times. In other studies, performing laboratory experiments, it has been noted that linear theory overestimates pressures [22] when in others predicted and measured boundary pressure show an excellent agreement [20]. To account for such discrepancies Suhayda [112] incorporates deformability of the seafloor to calculate bottom pressures through investigating the kinematics of surface

waves on a moving bottom. The author concluded that depending on the face angle between the two waves (surface and bottom boundary) bottom pressure can be either less (for in phase) or more (out of phase) than that predicted by linear theory. Also Mallard and Dalrymple [72] analyzed the effects of a deformable seafloor on dynamic pressure amplitudes and their analysis predicted higher pressure than those predicted by linear theory for rigid base. They concluded that dynamic response has an effect on very soft cohesive sediments and can be ignored for most sands [31].

5.5.2 Wave-induced stresses

Fung [34] has obtained wave-induced stresses utilizing Boussinesq's classical solution for a two-dimensional plane strain surface loading assuming a homogeneous semi-infinite elastic mass as:

$$\sigma_v = p_0(1 + \lambda z)\exp(-\lambda z)\cos(\lambda x - \omega t) \tag{5.22a}$$

and

$$\sigma_x = p_0(1 - \lambda z)\exp(-\lambda z)\cos(\lambda x - \omega t) \tag{5.22b}$$

and

$$\tau_{vh} = p_0 \lambda z \exp(-\lambda z)\sin(\lambda x - \omega t) \tag{5.22c}$$

where σ_v is the vertical normal stress, σ_h is the horizontal normal stress and τ_{vh} is the shear stress.

5.5.3 Wave-induced transient pore-water pressure

Putman [94] calculated the loss of wave energy due to percolation in permeable seafloors due to damping effects assuming incompressible flow, undrained conditions, saturated soil with rigid skeleton and hydraulic isotropy. Although wave-induced pore water pressure was implicit in his work he didn't give an explicit expression and Liu *et al.* [65] later published it based on Putman's work:

$$u = p_0 \frac{\cosh \lambda(h - z)}{\cosh \lambda h} \cos \lambda x - \omega t \tag{5.23}$$

Sleath [110] extended Liu *et al.*'s [65] expression to include hydraulic anisotropy:

$$u = p_0 \frac{\cosh \lambda(k_x/k_z)^{0.5}(h - z)}{\cosh \lambda(k_x/k_z)^{0.5} h} \cos(\lambda x - \omega t) \tag{5.24}$$

where k_x and k_z are permeabilities in x and z direction respectively. For $k_x = k_z$ equation 5.24 reduces to that of eq. 5.23.

5.5.4 Wave-induced residual pore-water pressure

Transient pore water pressures represent the immediate impact of wave-induced bottom pressure on the seafloor sediment. However, also residual excess pore water pressures are generated by the cyclic shear stresses arising from the dynamic wave pressures. Residual excess pore pressures represent the progressive built up of pore pressures due to wave action. Seed and Booker [104] published an empirical relationship for wave-induced excess pore water pressure:

$$u_g/\sigma'_{v0} = (2/\pi)\arcsin\left(N/N_l\right)^{0.5/\theta} \tag{5.25}$$

where u_g is the excess pore water pressure, N is the number of stress cycles during the storm, θ is an empirical constant ($\theta \approx 0.7$ for most sands [105]) and $N_f$is the number of cycles at a cyclic shear stress ratio of τ_{vh}/σ'_{v0} required to cause liquefaction. For practical purposes, the shear stress ratio $\tau_{vh}/\sigma'_{v0}$and N_f can be replaced by the stress ratio τ_e/σ'_{v0} and N_e which are the equivalents for regular instead of random waves of same duration. The stress ratio τ_e/σ'_{v0} can be calculated by taking the wave-induced bottom pressure defined in eq. 5.21 to calculate the shear stresses from eq. 5.22c and then divide by the overburden pressure σ'_{v0}

5.5.5 Slope stability

Henkel [50] used a limit equilibrium analysis with an assumed circular failure surface as shown in figure 5.5. He derived the following expression to determine the bottom pressure that causes failure:

$$\frac{\Delta p}{ky'L} = \frac{4\pi^2}{A}\left(\frac{x}{L}\right)^3(B - \beta/3k) \tag{5.26}$$

, where $A = \sin(\alpha) - \cos(\alpha)$; $\alpha = 2\pi x/L$; $B = (\sin(\theta) - \theta\cos(\theta))/\sin^3(\theta)$; $k = c_u/\gamma' z$; x, L and θ are defined in figure 5.5.

Rahman & Layas [95] presented an analytical procedure for evaluating the probability of wave-induced failure in terms of total stress. He treated both the waves and the shear strength of soils as random elements and he incorporated the associated uncertainties into the analysis.

Finn & Lee [30] and later Finn *et al.* [31] proposed an effective stress method of stability analysis based on Sarma's [100] method of slices (figure 5.5). A potential failure is assumed which may have any shape and the equilibrium of the sliding mass of unit thickness bounded by the failure surface and the surface of the slope is investigated. All acting forces are considered, including transient and residual pore-water pressures. Transient pore-water pressure can be calculated by equations 5.23 or 5.24, whereas residual pore-water pressures causing failure are sought in the slope stability analysis by setting the factor of safety to unity. The number of cycles N raising the residual pore-water pressure to a level that causes instability can be compared to the number of effective loading cycles considered equivalent to the wave loading to estimate the factor of safety.

Bea and Aurora [2] proposed a simplified method to get a first estimate of the factor of safety:

[**1**] Determine the maximum wave-induced shear stress using eq. 5.22c

[**2**] Multiply it by a plasticity factor to allow for inelastic and non-linear behavior; using finite element analysis, authors suggest values between 0.6 and 0.7.

[**3**] Compare with the undrained shear strength of the soil and determine a first approximation of the factor of safety.

5.6 Slope stability under earthquake loading

The most common procedure of analyzing slope stability under earthquake loading is the pseudo-static approach. Earthquake-induced acceleration is converted to an equivalent static

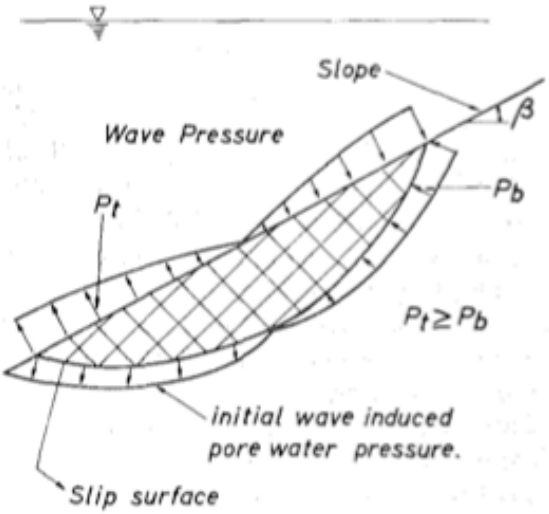

Figure 5.5: Sarma's [120] method of slices used by Finn & Lee [30] and Finn *et al.* [31] (source: Finn *et al.* [31]).

vertical and horizontal load generating normal and shear stresses respectively. As noted by Morgenstern [79] earthquake-induced normal stress is usually small and thus is ignored in the analysis, and only the horizontal force is considered which can drive the sediment to failure. Also, instead of the the actual acceleration response which is random and complex, an equivalent *characteristic* horizontal ground acceleration (k) is used which is assumed to be applied over such a long time that the induced stress can be considered constant.

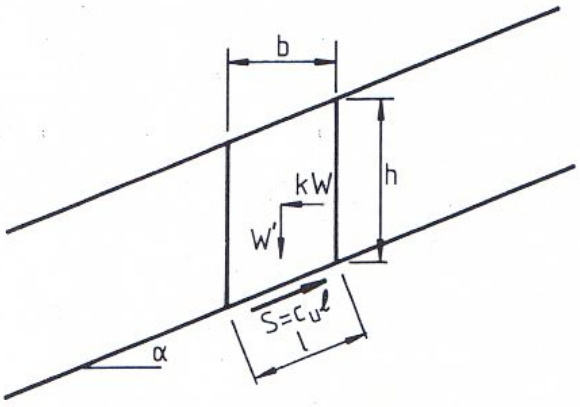

Figure 5.6: Simplified equilibrium of an infinite slope under undrained conditions under earthquake loading (source Poulos [92]).

Again, the infinite slope method is used and it is assumed that undrained conditions apply since marine sediments are not expected to drain immediately under earthquake loading. Equilibrium of forces on a submarine slope shown in figure 5.6 yields:

$$c_u l = W' \sin\alpha + kW \cos\alpha \tag{5.27}$$

which can be re-written in terms of the dimensionless shear strength as:

$$\frac{c_u}{\gamma' h} = (0.5 \sin 2\alpha + k \cos^2 \alpha \frac{\gamma}{\gamma'}) \tag{5.28}$$

The factor of safety for earthquake loading is:

$$F = \frac{c_u}{0.5\gamma' h \sin 2\alpha + k\gamma h \cos^2 \alpha} \tag{5.29}$$

For a typical sediment having $c_u/\gamma' h = 0.25$, a slope of 1^o requires only an acceleration of about 6% of gravity ($k = 0.06$) to cause failure [92]. It should be noted here that the seismic coefficient (k) is not equivalent to peak ground acceleration (PGA). The real seismic force is cyclic, changing direction with time, and its duration time is limited. Therefore, if one applies the maximum horizontal acceleration as a static force he would overestimate the earthquake-induced forces.

Instead of taking the undrained shear strength s_u equal to the cohesion c_u, Lee and Edwards [61] have proposed a different approach to evaluate the undrained cyclic shear strength, as:

$$s_{ur} = A_c A_r S(OCR)^m \tag{5.30}$$

where s_{ur} is the undrained shear strength under cyclic loading; OCR is the overconsolidation ratio (see section 2.1.2); m is a sediment property (≈ 0.8); S is the ratio of undrained shear strength to consolidation stress for normal consolidation (< 0.3 for clayey silt and clay and > 1.0 for sand and coarse silt); A_c and A_r are strength correction factors: A_c is a factor that accounts for the difference between the effects of isotropic-loading conditions in the laboratory and anisotropic loading in the filed and is typically equal to about 0.8; and A_r is the cyclic-strength degradation factor, which relates to the proportion of the shear strength that remains after earthquake shaking and resulting pore water pressure increase (< 0.5 for silt and > 1 for clay) [45].

Chapter 6

Tsunami wave generation

6.1 Intro

Tsunamis became the center of attention around the world after the 2004 Boxing Day tsunami in Sumatra, Indonesia with a death toll exceeding 280,000 (USGS [146]). It was notably the most international disaster of the past century and brought a lot of attention in the field of tsunami research. However, prior to this event, research had begun since the 50s, a few years after the 1946 Aleutian tsunami had struck Scotch Cap in Alaska and Hilo in Hawaii (Okal *et al.* [88]) and had come to an advanced level of numerical modeling since the 1980s. Two workshops in the early 90s marked the start of a new era in the field of tsunami modeling, that of Novosibirsk, Russia in 1989 (Gusiakov [42]) and another in Twin Harbors, Catalina Islands in the US in 1990 (Liu *et al.* [66]). These workshops started an international effort to advance the state of the art numerical codes. Numerical models in the 90s were able to perform two-directional depth averaged propagation and inundation/run-up computations. The same models, with minor advancements are still used today for tsunami forecasting. In terms of landslide generated tsunamis, the 1998 Papua New Guinea tsunami (e.g. Synolakis *et al.* [114]) became the landmark for extensive research in this specialized field of tsunami, as before that event the understanding of the mechanics of landslide tsunamis was very poor [115]. This event showed the hazard potentials of landslide tsunamis.

Tsunamis are long period waves of low steepness, generated by large-scale impulsive geophysical events such as submarine faulting, landslides (aerial and submarine), volcanic eruptions, asteroid impacts and atmospheric related impacts (rapid anomalous changes in the atmospheric pressure over the sea). The two most common triggers are earthquakes and submarine landslides; the other triggers are much less frequent but not less effective. The life of a tsunami can be divided in three phases: generation, propagation and inundation/run-up on shore. The generation phase involves the process of wave formation from the disturbance source. Propagation phase as the word implies involves propagation of waves in the sea. Inundation phase starts when the waves reach the coastline and start inundating on land. The quality of information available to define the source characteristics, also determine the quality of output data from tsunami propagation models. If the source information is poor then results will be poor (garbage in, garbage out), numerical models cannot do miracles.

In the following section the first phase of tsunami generation is analyzed for landslide and earthquake tsunamis and their differences are discussed.

6.2 6.2 Tsunami initial conditions

6.2.1 Earthquake-generated tsunami

Earthquake tsunamis are generated due to abrupt seafloor deformation arising from a seismic fault dislocation (figure 6.1). It is the vertical displacement of the seafloor due to the earthquake that produces the disturbance on the sea surface that in turn initiates tsunami propagation. Vertical displacement field is determined by the size of the earthquake given by the seismic moment (eq.4.1).

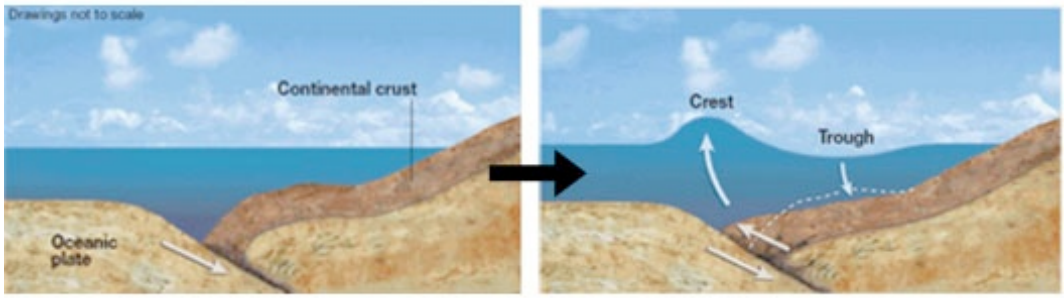

Figure 6.1: Tsunami generation due to submarine faulting (after Liu [145]).

The fault rupture area determines the horizontal extent of the seafloor vertical displacement field, whereas the amplitude of vertical displacement field is controlled by the fault slip $\Delta u$and the dip of the fault δ (figure 6.3). The fault slip Δu and fault dip Δu are two most important parameters controlling runup. As a rule of thumb, George Plafker's (USGS) observation in tsunami field surveys was that runup never exceeds twice the fault slip. The three parameters determining the size of the earthquake $(L, W, \Delta u)$ grow with the size of the earthquake in a matter that is not always predictable but in general follows some sort of principles called the *scaling laws*. For small earthquakes the seismic moment grows with the cube of the linear size of the earthquake $M_0 \approx L^3$, however as the width of the rupture area reaches the depth at which the earth ceases to be brittle, the earthquake size grows only with the rupture length $M_0 \approx L$ [89]. The smaller of the ratios $\Delta u/L$ *and* $\Delta u/W$ represents the stain released due to the fault rupture and is related to the strength of the rock, which ruptures at a certain strain ϵ_{max} [89]. Therefore, at large earthquakes Δu should stop growing once the rupture width stops growing to keep $\Delta u/W$ constant. In this context various authors have published empirical equations relating seismic moment with the rupture length, width, area and surface displacement (see for example Scholz [102] and Wells & Coppersmith [137]).

Typically the deformed area from the fault dislocation is in part uplifted and subsided. This has a direct effect on initial tsunami waveform, since sea-floor deformation is directly translated to the sea-surface. As a result of that, the coasts facing the subsided side of the fault will experience drawback of the sea first and a positive wave later, whereas coasts on the other side of the fault will experience elevation wave first. First real proof (anecdotal evidence previously existed) of the initial drawback of the sea, called *leading depression N-wave* (LDN) after Tadepalli & Synolakis [117] & [118] was provided by pictures taken at Manzanillo, Mexico after the $M_w = 8$ earthquake in October 1995 showing the Manzanillo Bay empty. This was earlier thought to be impossible since the depression wave; according to equation 5.16 should travel in smaller velocity than the elevation wave (leading elevation n-wave, LEN). However, tsunamis amplitudes in the deep ocean are in the order of centimeters and the difference in celerity is very small. Tadepalli & Synolakis [118] showed that waves generated from seismic

faulting would have to evolve more than once around the perimeter of the Earth for the LDN wave to overtake the LEN wave.

The sea-floor deformation due to an earthquake is complex, however in absence of detailed source models, deformation fields are evaluated with a relatively good accuracy using analytical formulae, such as that of Okada [86] for a finite rectangular fault assuming an elastic half-space, which is homogeneous and isotropic. Such analytical equations are used to get a good estimate of deformation field that can be used as initial conditions for tsunami modeling and forecasting in real time. In tsunami forecasting, time is very valuable and analytical equations have the advantage that seismic data available in short time after an earthquake event are enough to give an approximate solution. Analytical solutions neglecting homogeneity and isotropy of medium are available but require to be solved numerically (see Masterlark [74]). Also finite elements methods have been used to determine the deformation field due to fault dislocation but are out of the scope of this thesis.

After all input parameters required for an analytical model have been determined and a solution is obtained, initial conditions for tsunami modeling are usually determined by simply translating seafloor deformation directly to the sea-surface. This approach assumes static initial conditions and is based on the fact that fault rise time τ is very short and rupture velocity v ($1 < v < 10$km/s) is very fast compared tsunami propagation speeds (using eq. 5.17b for h = 5000m c $=\sqrt{gh}=$ 224m/s). However, there is a category of earthquakes called *slow earthquakes* ($0.1< v <1$ *km/s*) that consist of one or several high velocity rupture events, with long delays between successive events, accompanied by slip, which can contribute large amplitude low-frequency excitation [126]. The tsunamis produced from slow earthquakes are exceptionally large for the size of the earthquake. Todorovska and Trifunac [126] and more recent findings by Dutykh and Dias [24] have demonstrated that by taking into account the dynamic effects of rise time, initial waves can be amplified and the shape of wave train can be altered (see figure 6.2). The authors conclude that dynamic effects are important and should not be omitted from calculations. For all practical purposes, initial conditions are still determined with the static approach.

Okada's model

Input parameters for Okada's [86] model include material properties $\lambda$and μ (Lame's constants), which are usually kept constant, location (longitude and latitude), depth of hypocenter (h) and source characteristics, namely: fault mechanism (dip angle δ, strike ϕ and rake λ), rupture dimensions (length L and width W) and slip magnitude (Δu) as shown in figure 6.3(a). As an example, a deformation field produced using Okada's solution is shown in figure 6.3(b), surface projection of rupture area is shown with the black rectangle.

Application of Okada's model in tsunami modeling

This is an outline of how analytical formulas can be used to get the tsunami initial conditions in the case of an earthquake based on fault plane solutions:

[**1**] The epicenter can be calculated relatively fast with a relatively good accuracy depending on number and spatial distribution of seismometers that recorded the seismic waves.

[**2**] Focal depth is determined with good precision when a recording is available within a distance comparable to the focal depth. In many cases the focal depth is kept fixed at an arbitrary value during routine epicentral determinations. Otherwise if the earthquake

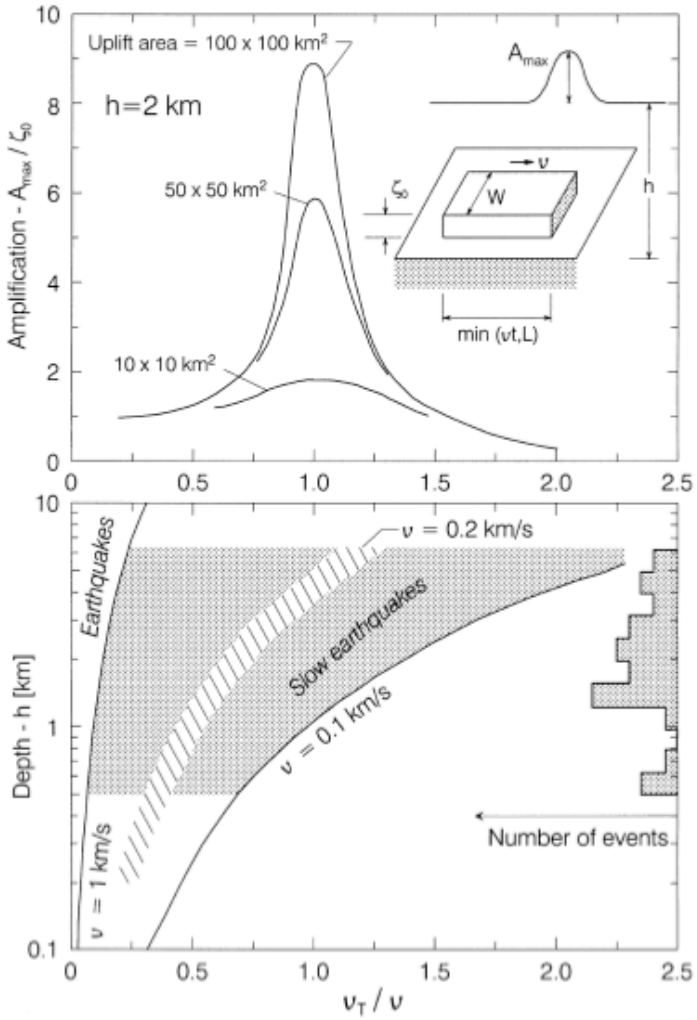

Figure 6.2: Top: amplification of the peak tsunami wave amplitude A_{max}/ζ_0, versus the velocity ratio v_T/v, for L = W = 10, 50 and 100 km and for h = 2 km (top). The similarity of the shape of A_{max}/ζ_0 with the amplitude of the relative response of a single-degree-of-freedom (SDOF) oscillator versus the frequency ratio ω/ω_N (ω is the forcing function circular frequency and ω_N is the oscillator natural frequency) is remarkable. The inverse of the area of the uplift of the ocean floor, 1/(LW), plays the role of the damping ratio. Bottom right: a histogram showing ocean depths for tsunamigenic earthquakes off the coast of Japan between 1931 and 1968. Bottom left: on the vertical axis is the ocean depth, h, and on the horizontal axis the velocity ratio v_T/v (where $v_T = \sqrt{gh}$). The solid lines show h versus v_T/v for v 0.1 and 1 km/s. The grey zone shows the range of depths and of v_T/v for slow earthquakes, which can lead to amplification of the tsunami wave amplitudes. (after Todorovska and Trifunac [126]).

is of deep focus, focal depth can be determined from the difference in arrival times of P and pP seismic waves. Usually for earthquakes with crustal origin pP waves are difficult to recognize in the seismograph signal and are assigned an arbitrary value, traditionally 33km.

[**3**] Magnitude can be estimated relatively fast ($\sim$ 10min) using automated algorithms. The estimation is good up to a certain magnitude ($\sim$7.5), after that automated algorithms using scales such as surface wave magnitude M_s saturate and magnitude is typically underestimated. For that reason other magnitude scales have been introduced like the

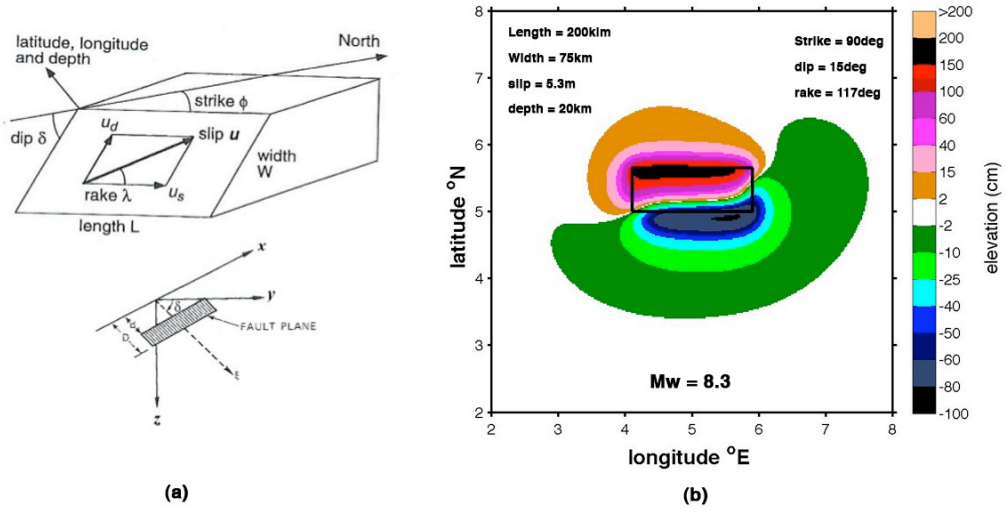

Figure 6.3: (a) Earthquake source parameters definition (MOST manual [76]). (b) Example of coseismic vertical displacement field using Okada's solution.

mantle magnitude M_m (Okal and Talandier [87]), to get earthquake magnitude fast without saturation.

[4] The tricky part is to determine the fault rupture length, width and slip given the data outlined above. Rupture area is usually estimated from aftershock distribution or/and by uplift/subsidence measurements in the field, if available. However, for quick estimates empirical scaling relations are used to determine rupture length, width and slip given the moment magnitude M_w (which is determined from other magnitudes using conversion relations). These equations assume an average constant slip, which is not the case in reality. Non-uniform slip distribution has been demonstrated by Geist and Dmowska [35] to have a significant effect on co-seismic vertical displacement and hence on the initial tsunami wave profile. While, Titov *et al.* [124] have demonstrated in a source sensitivity study that the details of the earthquake deformation are not important for inundation in the far-field, in the near-field slip distribution remains very important for inundation and runup distribution on shore.

For real time tsunami modeling other approaches have been proposed to constrain the source characteristics, the most significant being the inversion procedure developed by NOAA (National Oceanic and Atmospheric Administration). The details of this procedure are out of the scope of this thesis and interested readers should refer to Titov *et al.* [124] [125] and Wei *et al.* [135].

The most accurate means of determining seafloor deformation is to actually measure it in the field, by comparing the depth before and after the earthquake [115]. This requires high-resolution bathymetry data that is rarely available. Otherwise, if the fault rupture extends to the shore vertical displacements can be measured on land. The 1st of April 2007 Solomon Island earthquake provided the most detailed account of land level change datapoints up to date due to the unique setting of islands close to the ruptured fault (Fritz and Kalligeris [33]). The density and distribution of uplift and subsidence measurements for this event allow seismologists and tsunami modelers to determine the actual co-seismic vertical displacement field directly from the source and provides a unique opportunity to test tsunami numerical models. Such data are

not available in short time after the earthquake for tsunami forecasting but is very useful for post-tsunami research.

6.2.2 Submarine Landslide-generated tsunami

Submarine landslide tsunamis are generated due to the drawn down of a sliding mass on the seafloor as shown in figure 6.4. The sliding mass pushes the water forward producing an *LEN* wave propagating towards deep water and also produces an *LDN* wave propagating towards the shore due to the drop down movement. Compared to earthquake-generated tsunamis where rise is considered instantaneous, in the case of submarine landslides the sliding mass travels in speeds comparable to tsunami propagation speeds, thus requiring to define initial conditions in a dynamic approach. Also, initial conditions depend on initiation depth since it influences the amount of potential energy released form the slide that is transformed to wave energy. In addition, the landslide dimensions are not known until the seafloor is mapped using high-resolution multibeam sonar and multichannel seismic reflection data. Many tsunamis being allegedly generated by submarine landslides have not been examined thoroughly, usually due to the difficulty of mapping the seafloor to determine the dimensions of the slide.

Submarine landslides had been long recognized as a major tsunami trigger. Gutenberg [43] in 1939, based on earlier work by Milne and Verbeck, suggested that "submarine landslides are to be considered at least as one of the chief causes, if not indeed the major cause of tsunamis". Despite the 1958 catastrophic landslide that generated a massive tsunami in Lituya Bay, Alaska, amongst other events, earthquake induced seafloor deformation was widely believed to be the primary cause of most tsunamis until recently. It was the 1998 Papua New Guinea tsunami (Synolakis *et al.* [114]) that really shook the tsunami scientific community. The PNG tsunami highlighted the importance of landslide-triggered tsunamis and initialized a significant effort to better understand landslide waves within the context of long wave theory [116].

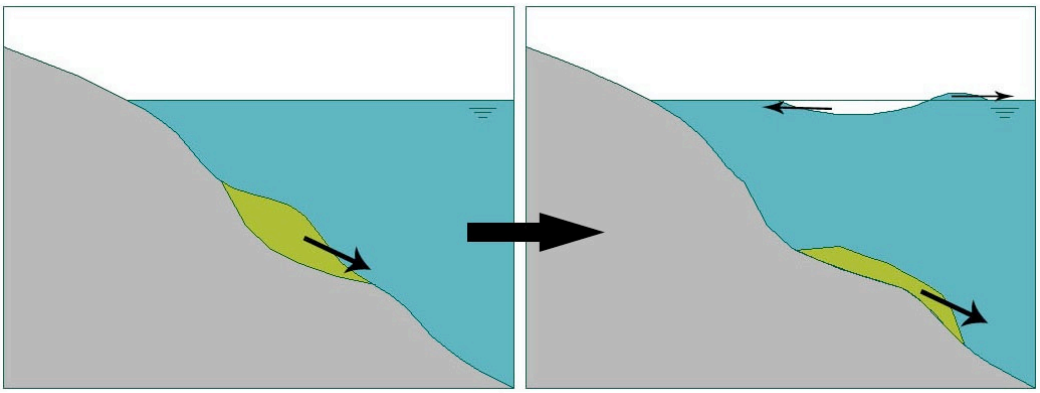

Figure 6.4: Tsunami generation due to submarine slope failure.

Still today, the mechanisms of tsunamis generation by submarine landslide are not as well understood as for waves generated by earthquakes. In this thesis, some of the most important empirical and computational methods to generate one, two and three-dimensional surface waveforms are discussed.

6.2.3 Empirical formulae

In the empirical equations that follow, authors used different symbols for the dimension parameters. In the present work, to avoid confusion I tried to use the same symbols for the same parameters.

Wiegel (1955)

Wiegel [138] in 1955, in order to gain some insight to submarine landslide tsunami generation, he performed a laboratory study using bodies of several shapes and weights dropped both vertically and sliding down inclines of several angles in water of various depths. He recognized that the magnitude of the amplitudes depended primarily upon the submerged weight of the body, but also upon the depth of submergence and the water depth.

Murty (1979)

Murty [81], based on the work by Streim and Miloh [111] and the experiments of Prins [93] (see section 6.2.4) proposed an energy method to acquire a certain wave height for a submarine landslide-generated solitary wave. He calculated the potential energy of submarine slide as shown in figure 6.6, of width w, thickness T and length L along the incline. D, D_0, D_s are the local depth, the depth of the end of the slope, and the depth at the center of gravity of the slide respectively (figure 6.5). The potential energy released by the landslide is given by:

$$E_p = gLwT(\rho - \rho_0)(D_0 - D_s) \tag{6.1}$$

where ρ, ρ_0 are the body and fluid densities.

The energy of a solitary wave is given by:

$$E_w = \frac{g\rho_0}{8\sqrt{3}} \, (\eta D)^{3/2} \tag{6.2}$$

Assuming that a fraction of the potential energy released by the landslide is converted to wave energy he derived an equation that gives an estimate of the wave height H as:

$$H = \frac{1}{D} \, [4\sqrt{3}\mu LT(\gamma - 1)(D_0 - D_s)]^{2/3} \tag{6.3}$$

where γ is the specific gravity. The factor μ is the percentage of potential energy assumed to contribute to wave generation. Wiegel's [138] experiments suggested that $\mu \ll 1$ and Murty [81] proposed a value of $\mu = 0.01$ for the case of Kitimat Inlet, British Columbia. Eq. 6.3 is valid provided that $D_s \leq D \leq D_0$.

Pelinovsky and Poplavsky (1996)

Pelinovksy and Poplavsky [91] proposed a hydrodynamic model based on linear potential theory for an inviscid fluid. They first linearize the hydrodynamic equations assuming flat bottom for simplicity, and then assign a certain hydrodynamic source describing the landslide movement, that of a Rankine ovoid shape. Continuity equation takes the form:

$$\frac{\partial^2 \Phi}{\partial x^2} + \frac{\partial^2 \Phi}{\partial y^2} + \frac{\partial^2 \Phi}{\partial z^2} = q(x, y, z, t) \tag{6.4}$$

For a Rankine ovoid, q is given by:

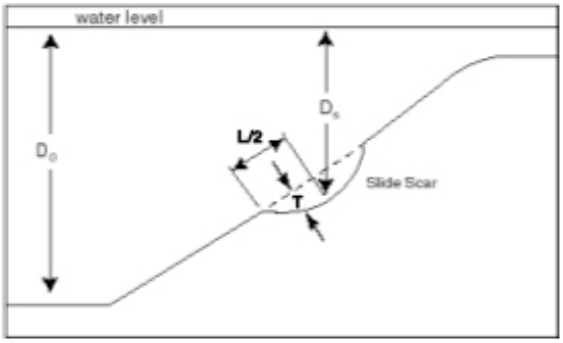

Figure 6.5: Parameters for Murty's [81] equation. (altered from image taken from Borrero [9])

$$q = \pi T^2 U[\delta(x - L - Ut) - \delta(x - Ut)]\delta(y)\delta(z + D) \tag{6.5}$$

where D is the water depth, U is the speed of the landslide movement, T is the height and L is the length (same symbols used here as before), and is the Dirac delta function.

Boundary conditions at the sea bottom and free surface are described by:

$$\frac{\partial \Phi}{\partial z} = 0 \tag{6.6a}$$

$$\frac{\partial^2 \Phi}{\partial t^2} + g\frac{\partial \Phi}{\partial z} = 0 \tag{6.6b}$$

The expression for q is valid if the Froude number (ratio of the body speed to the speed of long waves: $Fr = U^2/c^2$) is not close to 1. The authors focus on the steady state part of the solution, and in the case where water displacement will be significant, i.e. for large values of Froude number ($U \ll c$), they come up with the maximum free surface displacement at the point above the landslide center as:

$$\eta_m = \frac{T^2 L}{2D} \sum \frac{(-1)^2}{(2n + t)\sqrt{L^2/4 + (2n + 1)^2 D^2}} \tag{6.7}$$

In the case $L \ll D$, eq. 6.7 becomes:

$$\eta_m = \frac{\pi T^3}{4D} \tag{6.8}$$

Harbitz [48] had published the force balance on a body moving in a fluid on an inclined surface having a slope angle , along the coordinate x and equalized the rolling down force F_g to the sliding friction force F_f and the hydraylic resistance force F_h:

$$F_f = (\rho - \rho_0)\mu g V \cos\theta \tag{6.9a}$$

$$F_h = \rho C_D S U^2/2 \tag{6.9b}$$

$$F_g = (\rho - \rho_0) g V \sin\theta \tag{6.9c}$$

where ρ, ρ_0 are the body and fluid densities, $V = LS$ is the body volume, S is the cross section facing the direction of motion, C_n is the Coulomb friction coefficient and C_D is the drag coefficient.

Substituting $\rho_0 V$and $\rho V$with the masses m_0 and m_b respectively, equations 6.9a-6.9c lead to the following equation of motion :

$$m_b \frac{dU}{dt} = F_g - F_k - F_f \Rightarrow m_b \frac{dU}{dt} = (\rho_b - \rho_0) g V (\sin\theta - C_n \cos\theta) - \frac{\rho_0}{2} C_d S U^2 \tag{6.10}$$

Then, Pelinovksy and Poplavsky [91], based on eq.6.10, derived an equation describing the motion of a submarine landslide along an inclined seabed.

The P. Watts's method

Underwater slides

Watts [129], [130] also worked on the force balance of a submerged solid block along a straight incline but added the force of the added mass ($F_A = C_m m_0 (ds^2/dt^2)$). Adding the extra force and substituting $dU/dt = d^2s/dt^2$ and $S = Lw\sin\theta$ (for right triangle), eq. 6.10 becomes:

$$(m_b + C_m m_0) \frac{d^2 s}{dt^2} = (m_b - m_0) g (\sin\theta - C_n \cos\theta) - 0.5 C_d \rho_0 w L \sin\theta (\frac{ds}{dt})^2 \tag{6.11}$$

Initial accelaration at $ds/dt = 0$ is:

$$\alpha_0 = \frac{(m_b - m_0) g (\sin\theta - C_n \cos\theta)}{(m_b + C_m m_0)} \tag{6.12}$$

Terminal velocity is defined at the point where the slide mass stops accelerating ($d^2s/dt^2 = 0$):

$$u_t = \sqrt{\frac{2(m_b - m_o) g (\sin\theta - C_n \cos\theta)}{C_d \rho_0 w L \sin\theta}} \tag{6.13}$$

By integrating eq. 6.11 velocity and position as functions of time are derived as:

$$u(t) = u_t \tanh \frac{\alpha_0 t}{u_t} \tag{6.14a}$$

$$s(t) = \frac{u_t^2}{\alpha_0} ln[\cosh(\frac{\alpha_0 t}{u_t})] \tag{6.14b}$$

By letting C_m= 1, $C_n = 0$ and substituting $m_b = g\rho_0 V$ and $m_0 = \rho_0 V$ (where is the volume of the sliding mass, for right triangle $V = L^2 w/4$) equations 6.12 and 6.13 can be reduced to:

$$\alpha_0 = \frac{\gamma - 1}{\gamma + 1} g \sin\theta \tag{6.15a}$$

$$u_t = \sqrt{\frac{gL(\gamma - 1)}{2C_d}} \tag{6.15b}$$

For a semi-ellipse solid block ($S = wT$, $V = \pi L w T$), Grilli and Watts [37] derived the terminal velocity as:

$$u_t = \sqrt{0.5gL\pi \sin\theta(\gamma - 1)/C_d} \tag{6.16}$$

Characteristic length and time are defined as:

$$s_0 = \frac{u_t^2}{\alpha_0} \tag{6.17a}$$

$$t_0 = \frac{u_t}{\alpha_0} \tag{6.17b}$$

Underwater slumps

Watts *et al.* [131] and Grilli & Watts [37] model slumps as a rigid body rotating along a circular arc subject to external moments from added mass, buoyancy, gravity, and a constant residual stress. In equation of motion (eq. 6.11) if one sets $C_d = 0$ (because the angular rotation of slumps is small and hence the influence of fluid dynamic drag is often negligible), $s = R(\Phi - \Phi_i)$ (displacement equals to curvarture times angular displacement) and $\sin\theta \approx -\sin\Phi \approx -\Phi$ (small angle approximation) the equation of motion becomes:

$$R(m_b + C_m m_0)\frac{d^2\Phi}{dt^2} = (m_b - m_0)g(\Phi - C_n \cos\theta) \tag{6.18}$$

where R is the radius of curvature of the slump and is approximated in (Watts *et al.* [134]) as:

$$R = \frac{L^2}{8T} \tag{6.19}$$

Characteristic distance and time of motion are given by:

$$s_0 = \frac{R(\Phi - \Phi_i)}{2} = RC_n \cos\theta \tag{6.20a}$$

$$t_0 = \sqrt{\frac{R(\gamma + C_m)}{g(\gamma - 1}} \tag{6.20b}$$

Substituting equations 6.20a&6.20b in eq.6.18 leads to:

$$t_0^2\frac{d^2\Phi}{dt^2} + \Phi = C_n \cos\theta \tag{6.21}$$

For slumps starting at rest with $\Phi = \Phi_i$ and $\Phi = 0$ at $t = 0$, yiels:

$$s(t) = s_0(1 - \cos(\frac{t}{t_0})) \tag{6.22}$$

Initial conditions approximation

Watts *et al.* [134] derived their characteristic 2-D tsunami amplitude for underwater slides and underwater slumps respectively as:

$$\eta_{2d} = s_0(0.0574 - 0.0431\sin\theta)(\frac{T}{L})(\frac{L\sin\theta}{D})^{1.25}(1 - e^{-2.2(\gamma-1)}) \tag{6.23a}$$

$$\eta_{2d} = s_0\Delta\Phi^{0.39}(\frac{T}{L})(\frac{L\sin\theta}{D})^{1.25}(\frac{L}{R})^{0.63}(\frac{0.131}{\sin\theta})(1.47 - 0.35(\gamma - 1))(\gamma - 1) \tag{6.23b}$$

The 3-D dimension wave-shape generated by a submarine landslide is described by a double Gaussian function (dipole) of the form described in Watts *et al.* [131] and Borrero [9]:

$$\eta(x,y) = \frac{w}{\lambda + w}\ \mathrm{sech}^2(\frac{3y}{w+\lambda})[-1.2Z_{min}e^{-(1.2Z_{min}\frac{X-X_{min}}{Z_{max}\lambda})^2} + Z_{max}e^{-(\frac{X-X_{min}-\Delta X}{\lambda})^2}] \tag{6.24}$$

where:

$X_{min}$is the x-location of maximum drawdown:

$$X_{min} = 0.95(X_g + 0.4338 s_0 \cos\theta) \tag{6.25}$$

, where $X_g = (D + T/cos\theta)/\tan\theta$ as shown in figure 6.6.

ΔX is the distance between maximum drawdown and maximum elevation of the wave:

$$\Delta X = 0.5 t_0 \sqrt{gD} = 0.5\lambda \tag{6.26}$$

Z_{min} is the value of maximum drawdown:

$$Z_{min} = 2.1\eta_{2d} \tag{6.27}$$

Z_{max} is the value of maximum elevation wave:

$$Z_{max} = 0.64\eta_{2d}(0.8 + \frac{0.2D}{L\sin\theta}) \tag{6.28}$$

λ is the tsunami wavelength given by:

$$\lambda = t_0\sqrt{gD} \tag{6.29}$$

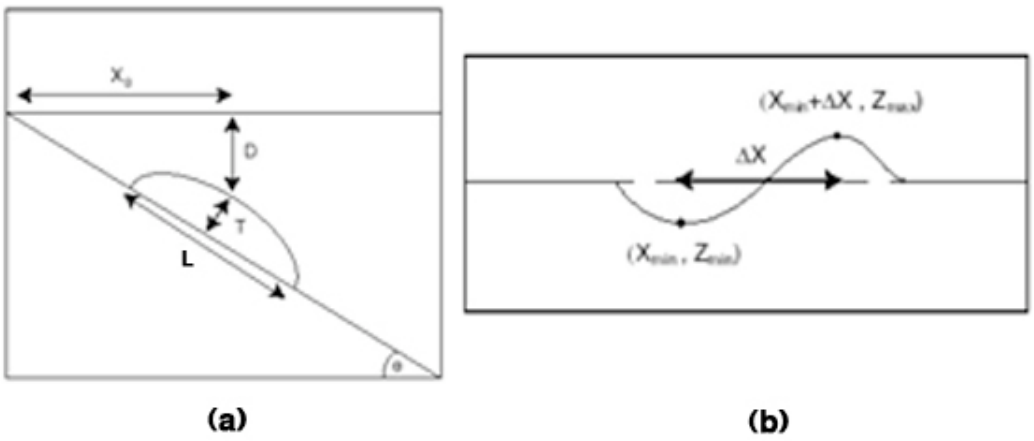

Figure 6.6: Parameters involved in Watts [129],[130] method (altered from figures taken from Borrero [9]).

PNG initial conditions

Given the landslide dimensions, one can derive explicitly approximate initial conditions for tsunami generation. Watts *et al.* [131] derived a double Gaussian function, based on the methodology described above, to model the 1998 PNG landslide-generated tsunami that was also subsequently used by Synolakis *et al.* [114]. According to Watts *et al.* [131] the dimensions of the slump as inferred from geological data, used in their model are shown in table 6.1

Table 6.1: Dimensions of the 1998 PNG slump (after Watts *et al.* [131] and Synolakis [115]).

Width w (km)	Length L (m)	Thickness T (m)	Local depth D (m)	Slope angle θ (^{o})	Specific gravity γ	Radius of curvature R (km)	Angular displacement (rad)
4	4.5	600	1000	8.95	2.15	7	0.286

Setting the mass coefficient $C_m = 1$ the characteristic distance and time of slump motion are:

$s_0 = 1$km (eq. 6.20a) and
$t_0 = 44.2$ s (eq. 6.20b)

Initial acceleration and maximum velocity are:

$a_0 = s_0/t_0^2 = 1000/44.2^2 = 0.51\ m/s^2$ (eqs. 6.17a & 6.17b) and
$u_{max} = s_0/t_0 = 23$m/s

Equation 6.23b gives the 2-D tsunami amplitude:

$\eta_{2d} = 41.0$m

Tsunami wavelength is calculated from eq. 6.29 as:

$\lambda = t_0\sqrt{gD} \approx 4.4$ km

The parameters of the double Gaussian function are:

$\Delta X = 0.5\lambda \approx 2.2$ km (eq.6.26)
$X_g \approx 10$km
$X_{\min} = 0.95(X_g + 0.4338 s_0 \cos\theta) \approx 9.9$ (eq. 6.25)
$Z_{\min} = 2.1\eta_{2d} = 2.1 \cdot 41.0 \approx 86.1$ m (eq. 6.27)
$Z_{\max} = 0.64\eta_{2d}\left(0.8 + \frac{0.2D}{L\sin\theta}\right) \approx 28.66$ m (eq. 6.28)

Finally, substituting in equation 6.24 one gets the initial conditions described by the approximation of a double Gaussian:

$$\eta(x,y) = \mathrm{sech}^2(\frac{3y}{8.4})[-49.2e^{-(0.6713(X-9.9-X_0)^2)} + 13.65e^{-0.0517(X-12.1-X_0)^2}] \tag{6.30}$$

which is different than what Watts *et al.* [131] derived in their work:

$$\eta(x,y) = \mathrm{sech}^2(\frac{3y}{8.4})[-35.71e^{-(0.10128(X-29.066-X_0)^2)} + 25.14e^{-0.0517(X-31.709-X_0)^2}] \tag{6.31}$$

Figure 6.7 shows the sea surface contours (2m interval) 44s after the beginning of the slumping event derived from eq.6.31, and superimposed is the color-shaded maximum tsunami amplitudes.

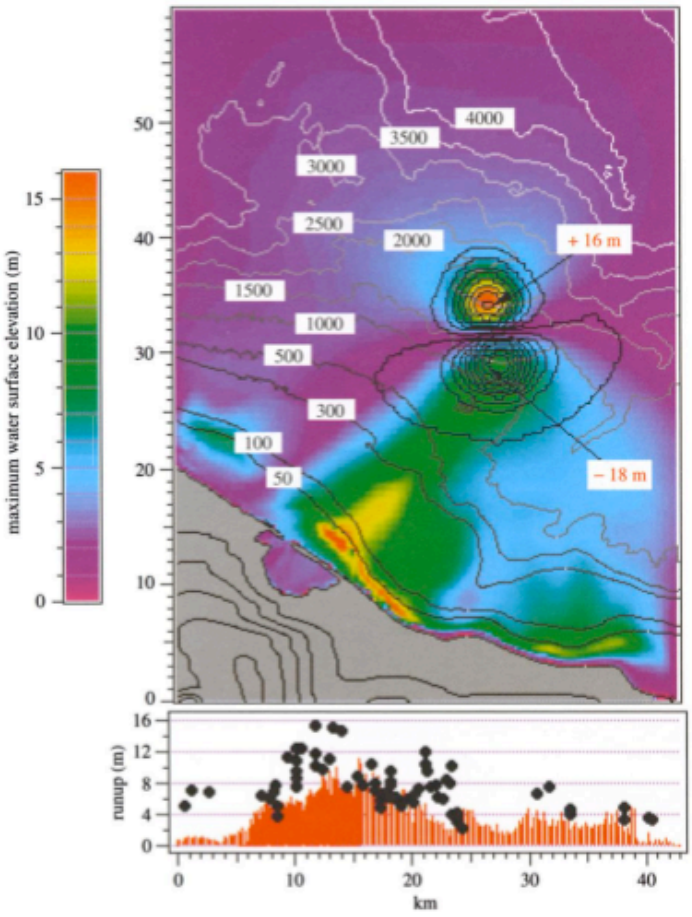

Figure 6.7: The computed waveshape for the 1998 PNG slump model. Initial conditions is plotted in black colored contours and superimposed is the maximum tsunami amplitude. Bottom: maximum run-up along coast line (red bars), compared with measured values (black dots) (after Synolakis *et al.* [114]).

Drawback of the P. Watts method is that equations 6.24-6.28 described in Borrero [9] have not been published and Watts *et al.* [131] do not explain in detail how all the parameters were derived to get to their dipole equation that was used as initial conditions for the simulation of the 1998 PNG tsunami. In addition, the 2-D tsunami amplitude equations described in Watts and Borrero [133] are slightly different than the ones described in Borrero [9] and Watts *et al.* [134], yielding different results. Finally, Watts *et al.* [134] propose slightly different double Gaussian function than the one described here (eq. 6.24) and in Borrero [9], but not all parameters are explicitly defined and was not employed here. They also refined the dimensions given in table 6.1, which yield different results in their case study for the 1998 PNG tsunami.

Synolakis (2003)

Synolakis [115] argued that Murty's [81] and Bohannon & Gardner's [8] (unpublished at the time, see below) methods need estimates for both an arbitrary specification of the drop of the slide, and the energy transfer coefficient μ.

Based on analytical results and laboratory observations, Synolakis [115] assumed that the initial wave is generated within a slope–parallel motion of less than half the slide length and proposed that the energy transfer is similar to that of a wavemaker within a time

$$t_0 = (1/4)^{1/3}\sqrt{D/g}(g/\alpha_0)^{1/3} \tag{6.32}$$

where α_0 is defined in eq. 6.15a.

He then calculated the net energy in an isosceles N–wave with height H and sech–like transverse shape as

$$\epsilon = \frac{2}{5}\sqrt{3}\pi\rho g w(DH)^{3/2} = (1/2)\rho g L T \Delta z \tag{6.33}$$

with a drop in height:

$$\Delta z = (1/2)\alpha_0 t_0^2 \sin\theta \tag{6.34}$$

By substituting 6.32 and 6.34 into 6.33, Synolakis [115] derived the maximum wave height as:

$$H = 0.139(\frac{L^2T^2}{D})^{1/3}(\frac{\alpha_0}{g})^{2/9} \tag{6.35}$$

The height of the depression wave is equal to the height of the elevation wave and does not rely on any assumptions on the transfer coefficient μ or any fitted empirical factors.

Bohannon and Gardner (2004)

Bohannon and Gardner [8] proposed another energy-based equation similar to Murty's [81], for a landslide of volume LTw and dropping height Δz to calculate maximum tsunami amplitude. The authors used the same potential energy equation (eq. 6.3) but instead of using the wave energy of a solitary wave they used an equation based on work by Watts [130]:

$$E_w = \rho_0 w \lambda H^2 \tag{6.36}$$

Again, combining eq. 6.3 and eq. 6.36 and assuming that a fraction mu of the potential energy released by the landslide is converted to wave energy he derived an equation that gives an estimate of the wave height H as:

$$H = \sqrt{\frac{\mu(\gamma-1)LT\Delta z}{\lambda}} \tag{6.37}$$

where λ is the predicted tsunami wavelength.

6.2.4 Computational methods and laboratory experiments

All the aforementioned empirical formulae give a different estimate of the maximum initial wave height of a submarine landslide-generated tsunami (figure 6.8). Obviously there is a lot of confusion when trying to use these formulae, not knowing which one gives the best estimate since up to present there hasn't been done any unified validation of all the formulae with numerical and experimental data. In this section some of the most important publications on numerical modeling and laboratory experiments of landslide-generated tsunami generation are discussed, which can provide useful data in understanding the parameters that control tsunami generation.

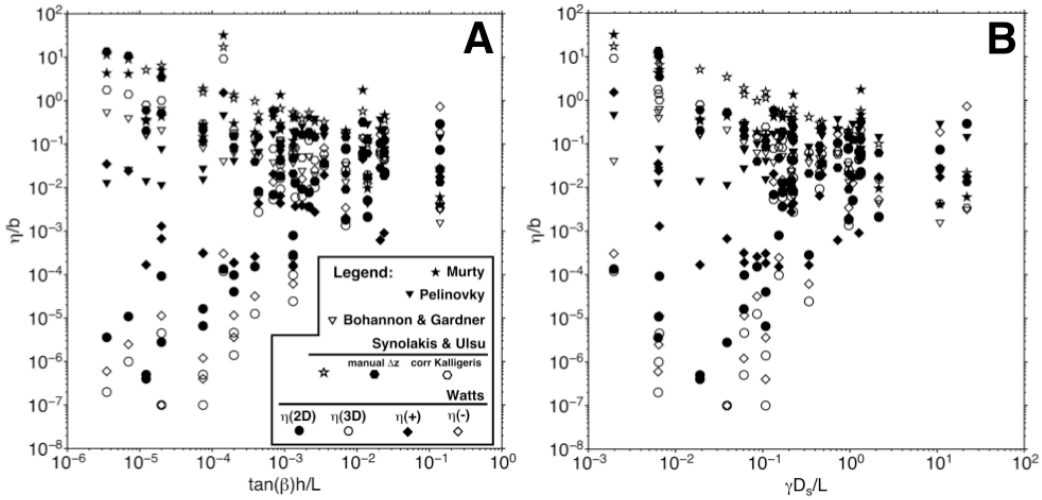

Figure 6.8: Scaled initial wave height predictions (ordinate) for a given landslide and two different scalings (abscissa); different symbols correspond to different empirical formulae (after Weiss and Synolakis (2010) unpublished work).

Laboratory experiments

Wiegel [138] conducted the first landslide tsunami experiments that we know in a 60ft (18.3m) long, 1ft (0.3m) wide and 3ft (0.91m) deep wave channel in University of California, Berkeley. He simulated landslides using a submerged wooden box with triangular cross-section to slide freely down an incline with 1/1 slope. That experiment using the wedge-type solid block set the standards for the experiments to follow.

A year later, Prins [93] studied water waves generated by an initial rectangular elevation or depression over a region of the free surface propagating down a constant depth channel [130]. Because Prins [93] studied water waves generated by a net volumetric displacement of water, solitary waves were observed to emerge from the wave train during some of the experiments, which influenced the work of Striem & Miloh [89] and subsequently Murty's [81] work [130].

Heinrich [49] conducted one underwater experiment using a solid wedge model on a 1:1 slope and then used a 2-D finite difference solution of the Navier-Stokes equations to compare his model results with the laboratory data. He found exceptional agreement, with largest discrepancy just after sliding initiation, where turbulence is the largest.

The wedge-shaped model was also used in the experiments of Watts [129],[130],[132] at Caltech, Pasadena and in the large scale experiments of Raichlen and Synolakis [96] at the Oregon State's University 104m long, 3.66m wide and 4.47m deep wave channel with 1:2 plane slope located at one end of the tank. This experiment described in Liu *et al.* [68] became the

benchmark to validate runup models. Liu *et al.* [68] also compared the Oregon experiments of Raichlen and Synolakis [96] to the results from numerical modeling using a Navier-Stokes code and got a good match, but with huge computational cost. Images from the experiment and the Liu *et al.*'s [68] numerical model are shown in figure 6.9.

More recently, Enet and Grilli [26] conducted large-scale 3-D laboratory experiments using idealized Gaussian-shaped rigid slides moving down a 15^o slope to provide more experimental data for model validation.

Computational methods

Jiang and LeBlond [55] treated landslides as a laminar flow of an incompressible viscous fluid with an initial shape of parabola, perched on an inclined plane. The slide mass was free to deform as it moved downslope. Their solution was based on 2+1 depth averaged shallow water equations. They noted the time-dependence of initial conditions.

Grilli *et al.* [38] employed the 3D potential flow solver of the Navier–Stokes equations using a Boundary Element Method (BEM) developed by Grilli *et al.* [39] to calculate the waves generated by a moving submerged mass. Studying the effect of landslide width on generated tsunami, they concluded that the 2-D approximation is applicable when the ratio of landslide width over length is greater than two. Lynett and Liu [56] derived a depth–integrated formulation to model rigid landslides and validated their algorithm using Hammack's [44] experiments and with a boundary integral equation method model.

Liu *et al.* [67] proposed an exact solution to a forced linear wave equation for a rigid Gaussian-shaped slide and derived conclusions on the effects of the slope, slide length and thickness. Panizzo and Dalrymple [90] performed a fully coupled computation of both the slide and induced fluid motion, using the method known as smooth particle hydrodynamics (SPH) to model the 2-D motion the underwater solid wedge-type landslide.

The present state of the art in terms of modeling landslide-generated tsunami are the numerical models that simulate the flow of fluids and gases as well as deformations of solid bodies occurring at subsonic and supersonic speeds, called hydrocodes. Most hydrocodes have been developed at Los Alamos National Laboratory in the context of impact–crater research. Mader and Gittings [71] used a hydrocode called SAGE to model the Lituya Bay experiment of Fritz (Fritz *et al.* [32]). They got a phenomenal estimate of runup within 10%. Another hydrocode that was initially developed to simulate meteorite impact processes that has also has been used for tsunami research is iSALE (e.g. Weiss *et al.* [136]). It has been through many refinements and advancements since it was first develop and now the user can specify twenty material parameters to model the landslide motion and interaction accurately. However it is also a question of having the information to set the right parameters.

More recently, Abadie *et al.* [1] employed a multi-grid Navier–Stokes model to simulate the generation of tsunamis by subaerial deformable slide. They validated their code with experimental results for the generation of a solitary wave by a falling block. The influence of slide deformation on wave generation was studied by performing simulations for various slide viscosity, the largest one corresponding to a nearly rigid slide. They concluded that the deforming slide shape strongly influences both the slide motion and wave generation and should be included in numerical simulations of landslide tsunami, in order to improve the prediction of wave characteristics.

Hydrocodes by varying viscosity are able to simulate both rigid-like and fluid-like slides. However, it is very important to simulate correctly the transition from rigid to fluid-like behavior as the slide disintegrates moving downlope and the transition occurs at a very important point

for tsunami generation. Hydrocodes developed at Los Alamos have the advantage of using appropriate constitutive models to model the transition correctly.

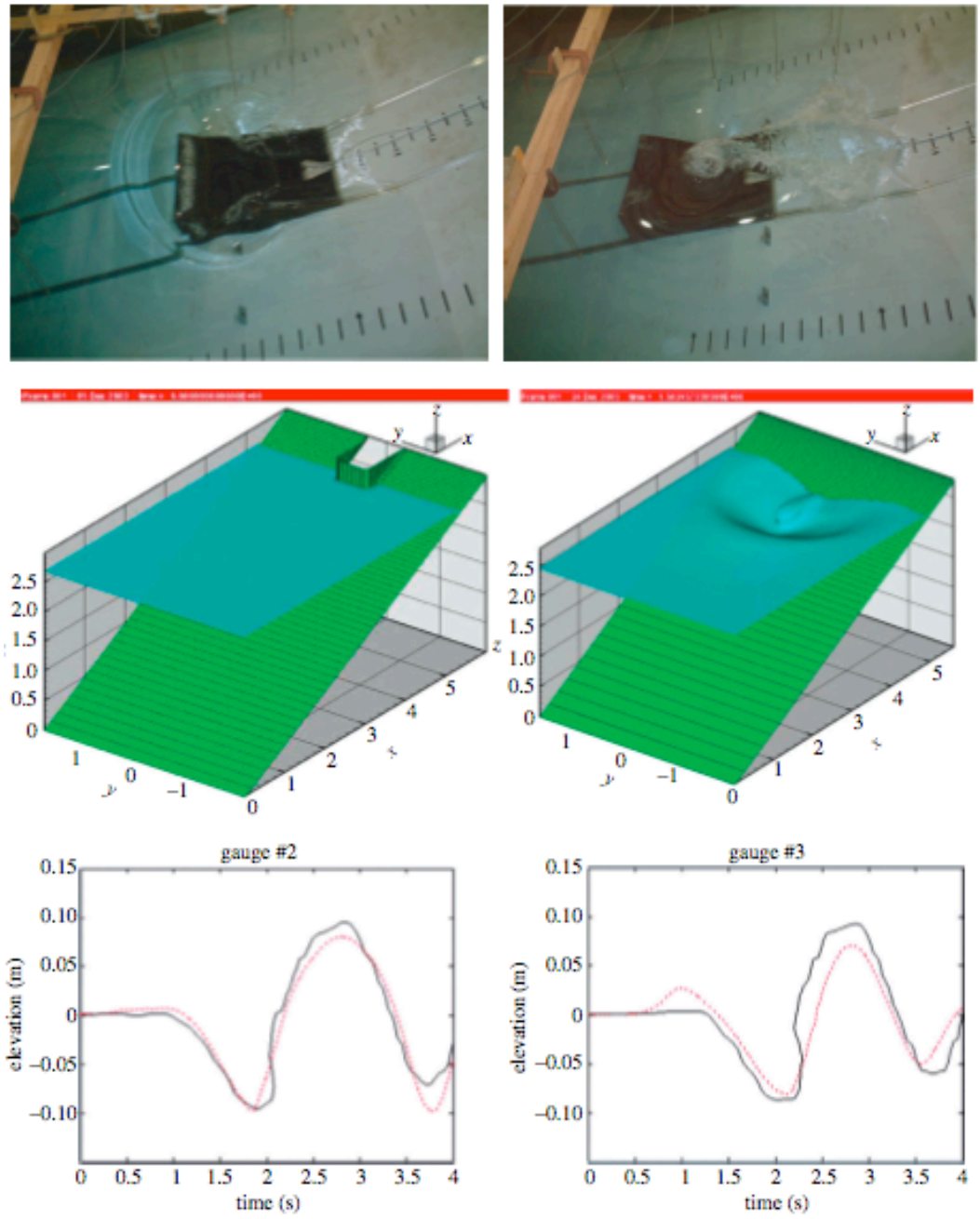

Figure 6.9: A moving wedge as a model of submarine landslide. (top, left) The initial wave from a submerged slide, immediately after motion started; note the LDN.(top, right) The wave about 1s later, as the run-up forms per Raichlen & Synolakis [96].(middle) Animation stills from Liu *et al.*'s [68] simulations as guided by the landslide experiments.(bottom) Comparison of laboratory measurements (solidline) with numerical predictions (dashedline) for the shoreline motion for two locations off the centerline from Liu *et al* [68] (after Synolakis and Bernard [116]).

Chapter 7

Conclusions

Various factors affecting underwater slope stability were presented here. Failure as was shown is initiated by reduction of the shear strength of the soil which decreases the resisting forces in the slope, or by the increase of the driving forces in the slope or by both.

Driving forces are principally due to gravity, but earthquakes and large water waves can also produce driving forces [140]. For slope stability analysis under earthquake loading the dynamic problem is converted to pseudostatic by introducing a characteristic horizontal acceleration (k).

Shear strength reduction of soils occurs due to pore water pressure rise generated by either (a) rapid sedimentation, (b) cyclic loading or (c) gas hydrate disassociation:

[**a**] Rapid deposition tends to generate excess pore water pressure in mostly under-consolidated soils, usually found in river deltas and fjords. The rate of deposition plays an important role, however failure can be initiated even for very low deposition rates at longer periods of time given that the consolidation coefficient is low.

[**b**] The source of cyclic loading in the marine environmental is commonly either hydraulic loads or earthquake loading, which are the major cause of landslides on the continental slopes.

- Hydraulic forces on the seabed may arise from tides, storm waves, currents or tsunamis. Shorter period waves affect the seabed stability at depths less than 150-300m, whereas longer period waves such as tides and tsunamis can have an impact at even greater depths.
- Cyclic loading due to earthquake induced ground motion, depending on the level and duration of cycled stress and also soil behavior, can result in continuos pore pressure rise, loss of shear strength and eventually liquefaction. Soils more susceptible to liquefaction are saturated cohesionless soils, for which true liquefaction can occur.

[**c**] Gas hydrate disassociation occurs under certain temperature and pressure conditions. The associated release of gas in the form of bubbles reduces the shear strength of the soil leading to failure in some cases.

Slope stability analysis was presented for the gravity, earthquake and hydraulic loading cases as well as for gas hydrate disassociation.

At the last chapter, an introduction was given to tsunami generation. For earthquake generated tsunamis, initial conditions are typically considered static. Analytical formulae, such as that of Okada [86] can be used with a relatively good accuracy to approximate the sea-floor deformaiton field to used as initial conditions for tsunami numerical models. On the other

hand, for landslide-generated tsunami, the downslope velocity of the failure mass is comparable to the propagation speed of tsunamis and thus the time scale has to be incorporated in the calculations leading to a dynamic solution. A set of empirical equations available in literature is given to derive 1-d, 2-d initial wave heights as well as 3-d surface waveforms, to be used as a proxy for landslide hazard studies.

Bibliography

[1] Abadie, S., Morichon, D., Grilli, S.T. and Glockner, S. (2008). VOF/Navier-Stokes numerical modeling of surface waves generated by subaerial landslides. *La Houille Blanche*, 1 (Feb. 2008), 21-26, doi:10.1051/lhb:2008001.

[2] Bea, R.G., Aurora, R.P. (1981), A simplified evaluation of seafloor stability, *Proc. 13th Annual OTC, Houston,* Paper OTC 3975, pp. 223-240.

[3] Bishop, A.W. (1955). The Principle of Effective Stress, Teknish, Ukefland. 106(39), pp. 359-383.

[4] Bishop A.W. & Skempton A. W. (1955). The gain in stability due to pore pressure dissipation in a soft clay foundation. *Proc. 5th Cong. Large Dams* **1**, 613-638.

[5] Bishop, A. W., and Morgenstern, N. R. (1960), Stability coefficients for earth slopes, *Geotechnique*, **10**, pp. 129-150.

[6] Bjerrum, L., Simons, N.E. (1960), Comparison of Shear Strength Characteristics of Normally Consolidated Clays, Proc. ASCE Research Conference on Shear Strength of Cohesive Soils, pp. 711-726.

[7] Bjerrum, L. (1973), Problems of Soil Mechanics and Construction on Soft Clays and Structurally Unstable Soils (Collapsible, Expansive, and Others), Proceedings, Eighth International Conference on Soil MechanicEngineering, Moscow, U.S.S.R., Vol. 3, pp. 111-159.

[8] Bohannon, G. B. and J.V. Gardner (2004), Submarine landslides of San Pedro Escarpment, southwest of Long Beach, California, *Marine Geology,* **203**, pp. 261-268.

[9] Borrero, J..C. (2001), Analysis of tsunami hazards in Southerm California, Ph.D. Thesis, University of Southern California, Los Angeles, California.

[10] Boulanger R. W. (2003), High overburden stress effects in liquefaction analyses, *J. Geotechnical and Geoenvironmental Engineering*, ASCE, 129(12), pp. 1071-1082.

[11] Boulanger, R. W. and I. M. Idriss (2004), State normalization of penetration resistance and the effect of overburden stress on liquefaction resistance, *Proc., 11th International Conf. on Soil Dynamics and Earthquake Engineering and 3rd International Conference on Earthquake Geotechnical Engineering*, Univ. of California, Berkeley, CA.

[12] Bugge T., Befring S., Belderson R.H., Eidvin T., Jansen E., Kenyon N.H., Holtedahl H. & Sejrup H.P. (1987), A giant three-stage submarine slide off Norway, *Geo-Marine Letters*, 7(4), DOI 10.1007/BF02242771.

[13] Craig R.F. (1997). Soil Mechanics, Spon Press.

[14] Cooper, R.G. (2007) Mass Movements in Great Britain, Geological Conservation Review Series, No. 33, Joint Nature Conservation Committee, Peterborough, 348 pp.

[15] Coulomb, C. A. (1776). Essai sur une application des regles des maximis et minimis a quelquels problemesde statique a la architecture. *Mem. Acad. Roy. Div. Sav.*, vol 7, pp 343-387.

[16] Cruden D.M. & Varnes D. J. (1996). Landslide types and processes, In: *Turner A.K.; Shuster R.L. (eds) Landslides: Investigation and Mitigation. Transp Res Board*, Spec Rep 247, pp 36–75.

[17] Dalrymple R A, Rogers B D. (2006), Numerical Modeling of Water Waves with the SPH Method, *Coastal Engineering*. Vol. 53. No. 2. pp. 141-147.

[18] Datta, M., Gulhati, S.K. & Rao, V.G. (1979), Crushing of calcareous sands during shear, Proc. 11th. offshore Technology Conf., Houston, pp. 1459-1467.

[19] Demars K.R., Nacci, V.A., Kelly W.E. Wang, M.C. (1976), Carbonate content an index property for ocean sediments, *Proc. 5th Annual OTC, Houston*, Paper OTC 2627, pp. 97-106.

[20] Demars K. R. & Vanover E.A. (1985). Measurement of wave-induced pressures and stresses in a sandbed. *Mar. Geotech.*, **vol. 6**, pp. 29-59.

[21] Dingle,R.V., (1977), The anatomy of a large submarine slump on a sheared continental margin (SE Africa), *J. Geol. Soc. London* 134 (3), pp. 293–310.

[22] Doyle, E. H. (1973). Soil wave tank studies of marine soil instability. *Offshore Technology Conference Preprints*, **vol. II**, pp. 753-766.

[23] Duncan J. M. and Wright S. G. (2005). Soil Strength and Slope Stability. John Willey & Sons, Inc., Hoboken, New Jersey.

[24] Dutykh, D. and F. Dias (2009). Tsunami generation by dynamic displacement of sea bed due to dip-slip faulting, *Mathematics and Computes in Simulation*, **Vol. 80**, pp. 837-848.

[25] Elnashai A. M. & L. Di Sarno (2008). Fundamentals of earthquake engineering, John Wiley & Sons, Ltd.

[26] Enet, F. and Grilli, S.T. (2007). Experimental Study of Tsunami Generation by Three-dimensional Rigid Underwater Landslides. *Journal of Waterway Port Coastal and Ocean Engineering*, 133(6), 442-454.

[27] Eskijian M.L., Heffron R.E., Dahlgren T., (2003), Engineering Standards for Marine Oil Terminals and other Natural Hazard Threats, *In: Submarine Landslides and Tsunamis,* Kluwer Academic Publishers, pp. 259-266.

[28] Evans N. C. (1995). Stability of submarine slopes. GEO REPORT No. 47, GEO Special Project Report No. SPR 4/94, Hong Kong Government.

[29] Field, M.E., and Edwards, B.D. (1980), Slopes of the southern California borderland: A regime of mass transport, in *Field, M.E., Bouma, A.H., Colbourn, I.P., Douglas, R.G., and Ingle, J.C., eds., Pacific Section SEPM, Pacific Coast Paleogeography Symposium*, No. 4, Los Angeles, Calif., pp. 169 184.

[30] Finn, W. D. L., and Lee, K. W. (1979), Seafloor Stability Under Seismic and Wave Loading, presented at the April 2-6, 1979, Soil Dynamics in the Marine Environment, ASCE National Convention and Exposition held at Boston, Mass., (Preprint 3604).

[31] Finn W. D. L., R. Siddharthan & G. R. Martin (1983). Response of seafloor to ocean waves, *J. Geotech. Engng.*, ASCE, **109**(4) pp. 562-572.

[32] Fritz, H.M., Hager, W.H., Minor, H.-E. (2001), Lituya Bay case: rockslide impact and wave run-up. *Science of Tsunami Hazards*, 19(1), pp. 3-22.

[33] Fritz H.M. and N. Kalligeris (2008). Ancestral heritage saves tribes during 1 April 2007 Solomon Islands tsunami. *Geophysical Research Letters*, **35**, L01607, doi:10.1029/2007GL031654.

[34] Fung Y. C. (1965). Foundations of solid mechanics. Englewood Cliffs, NJ: Prentice-Hall.

[35] Geist, E.L. and Dmowska, R. (1999). "Local Tsunamis and Distributed Slip at the Source", *Pure and Applied Geophysics*, **Vol. 154**, No. 3-4, pp. 485-512.

[36] Giani G. P. (1992). Rock slope stability analysis, Balkerma Publishers.

[37] Grilli, S.T., P. Watts (1999), Modeling of waves generated by a moving submerged body. Applications to underwater landslides, *Engineering Analysis with Boundary Elements*, 23(8), pp. 645-656.

[38] Grilli ST, Guyenne P, Dias F (2001), A fully nonlinear model for three-dimensional overturning waves over arbitrary bottom. Int J Numer Methods Fluids, 35(7), 829 ± 67.

[39] Grilli, S. T., Vogelmann, S., and Watts, P. (2002), Development of a 3D numerical wave tank for modeling tsunami generation by underwater landslides., *Eng. Anal. Boundary Elem.*, 26(4), pp. 301-313.

[40] Grilli S.T. and P. Watts (2005), Tsunami generation by submarine mass failure. I: Modeling, experimental validation, and sensitivity analyses, *Journal of Waterway, Port, Coastal and Ocean Engineering*, pp. 283–297

[41] Grozic, J.L.H. and Kvalstad, T.J. (2001). Effect of gas on deepwater marine sediments. *In* Proceedings of the XVth International Conference on Soil Mechanics and Geotechnical Engineering, August 27-31,2001, Istanbul, Turkey, pp. 2289-2294.

[42] Gusiakov, V. K. (1990). Tsunamis: their science and hazard mitigation. *Proc. International Tsunami Symposium International Union of Geodesy and Geophysics, Novosibirsk Computing Center*, USSR. Academy of Sciences, US Library of Congress Number 92–246716.

[43] Gutenberg, B. (1939), Tsunamis and Earthquakes, *Bull. Seismol. Soc. Am.,* 29(4), pp. 517-526.

[44] Hammack, H. L. (1973), A note on tsunamis: their generation and propagation in an ocean of uniform depth. *J. Fluid Mech.* **60**, pp. 769-799.

[45] Hampton M.A., Lee H.J. & Locat J., (1996), Submarine Landslides, *Reviews of Geophysics,*v. **34**, pp. 33-59.

[46] Hance, JJ, (2003), Development of a Database and Assessment of Seafloor Slope Stability based on Published Literature, Msc Thesis, University of Texas at Austin.

[47] Hanks, T.C. and H. Kanamori (1979), A moment magnitude scale, *J. Gephys. Res.,* **84**, No 85, pp. 2348-2350.

[48] Harbitz, C.B (1992), Model Simulations of tsunamis generated by the Storegga Slides, Marine Geology, 105, pp. 1-21.

[49] Heinrich, P. (1992), Nonlinear water waves generated by submarine and aerial landslides, *J. Waterway Port Coastal Eng.,* 118(3), pp. 249-266.

[50] Henkel, D.J, (1982), The role of waves in causing submarine landslides, *Geotechnique,* 20, pp. 75-80.

[51] Idriss, I.M. (1999), An update to the Seed-Idriss simplified procedure for evaluating liquefaction potential, *Proc., TRB Workshop on New Approaches to Liquefaction*, January, Publication No. FHWA-RD-99-165, Federal Highway Administration.

[52] Idriss I. M. and Boulanger, R. W. (2004), Semi-empirical procedures for evaluating liquefaction potential during earthquakes , *Proc., 11th International Conf. on Soil Dynamics and Earthquake Engineering and 3rd International Conference on Earthquake Geotechnical Engineering*, Univ. of California, Berkeley, CA. pp. 32-56.

[53] Iwasaki, S. (1982), Experimental study of a tsunami generated by a horizontal motion of a sloping bottom, *Bull. Earth. Inst.,* 57, pp. 239-262.

[54] Jacky, J. (1944). The Coefficient of Earth Pressure at Rest, Journal for Society of Hungarian Architects and Engineers, Budapest, pp. 355-358.

[55] Jiang I. and LeBlond, P.H. (1992), The coupling of a submarine slide and the surface waves which it generates, *J. Goephys. Res. Oceans,* 98 (C8), pp. 12731-12744.

[56] Kanamori H. (1972), Mechanism of tsunami earthquakes, *Phys. Earth Planet. Interiors*, **6**, pp. 346-359.

[57] Kanamori, H. (1977), The energy release in great earthquakes, *Journal of Geophysical Research*, **82**, pp. 2981-2987.

[58] Kvalstad T. J. (2009). Geohazards from seafloor instability and mass flow, *International Association of Oil & Gas Producers,* Report No. 425.

[59] Ladd, C. C, and Foott R. (1974). New Design Procedure for Stability of Soft Clays, *Journal of the Geotechnical Engineering Division*, *ASCE*, **vol. 100**, No. GT7, pp. 763-786

[60] Ladd C. C., Foott R., Ishihara K., Schlosser F. and Poulos H. G. (1977). Stress-Deformation and Strength Characteristics, *Proceedings of the Ninth Inter- national Conference on Soil Mechanics and Foundation Engineering*, Tokyo, Japan, **vol. 2**, pp. 421-494.

[61] Lee, H. J., and B. D. Edwards (1986). Regional method to assess offshore slope stability, *Journal of Geotechnical Engineering*, **112**, 489-509.

[62] Lee, H.J., Schwab, W.C. and Booth, J.S. (1993). Submarine Landslides: An introduction, in "Submarine Landslides: Selected Studies in the U.S. Exclusive Economic Zone, *U.S. Geological Survey Bulletin 2002*, U.S. Dept. of the Interior, Denver Co., 80225, 1-13.

[63] [6] Legros F. (2002). The mobility of long-runout landslides, *Engineering Geology,* v. **63**, pp. 301-321.

[64] Liao and Whitman, R. V. (1986), Overburden correction factors for SPT in sand, *Journal of Geotechnical Engineering*, ASCE, 112(3), pp. 373-377.

[65] Liu, P. L. F., Timothy, P., and O'Donnell (1979). Wave induced forces on buried pipelines in permeable seabeds. *Proceedings, 4th Conference on Civil engineering in the Oceans*, San Francisco, Calif., pp. 111-121.

[66] Liu, P. L.-F., Synolakis, C. E. & Yeh, H. H. (1991). Report on the internationalworkshop on long wave runup. *J. Fluid Mech.* **229**, pp. 675–688. (doi:10.1017/S0022112091003221).

[67] Liu, P. L.-F., Lynett, P. & Synolakis, C. E. (2003), Analytical solutions for forced long waves on a sloping beach. *J. Fluid Mech.*, **478**, pp. 101–109. (doi:10.1017/S0022112002003385)

[68] Liu, P.L-F., Wu, T-R,, Raichlen, F., Synolakis, C.E., Borrero, J, (2005), Runup and rundown generated by three–dimensional sliding masses, *Journal of Fluid Mechanics*, 536, pp. 107–144.

[69] Locat, J., & Lee, H. J. (2000). Submarine landslides: Advances and challenges, *In Proceedings of the 8th International Symposium on Landslides*, Cardiff UK.

[70] ynett, R. Liu P.-L. (2002), A numerical study of submarine-landslide-generated waves and run-up, **458**, A2002, pp. 2885-2910, doi:10.1098/rspa.2002.0973.

[71] Mader, C.L., and Gittings, M.L. (2002), Modling the 1958 Lituya Bay mega-tsunami, II: Science of Tsunami Hazards, v. 20, pp. 241-250.

[72] Mallard, W. & Dalrymple, R. A. (1977). Water Waves Propagating Over a Deformable Bottom, *Proceedings, Ninth Annual Off-Shore Technology Conference*, Houston, Tex., May, pp. 141-146.

[73] Mason D.G., Harbitz C.B., Wynn R.B., Pedersen G., Lovholt F., (2006). Submarine landslides: processes, triggers and hazard prediction, *Phil. Trans. R. Soc.* **364**, pp. 2009–2039 doi:10.1098/rsta.2006.1810.

[74] Masterlark, T. (2003), Finite element model predictions of static deformation from dislocation sources in a subduction zone: Sensivities to homogeneous, isotropic, Poisson-solid, and half-space assumptions, *J. Geophys. Res.* **108**, 2540.

[75] Mayne, P.W. and Kulhawy, F.H. (1982), K_0 - OCR relationships in soill, *Journal of Geotechnical Engineering*, Vol. 108 (GT6), pp. 851-872.

[76] Method of Splitting Tsunami (MOST) Software Manual (2006). Tsunami Research Program, Pacific Marine Environmental Laboratory, National Oceanic and Atmospheric Administration.

[77] Mitchel J. K. (1962). Components of pore water pressure and their engineering significance. Clays and Clay Minerals Volume 9. Proceedings of the *ninth national conference on clays and clay minerals,* pp 162-184. New York: Pergamon Press.

[78] Moore D. G. (1978). Submarine slides. *Rockslides and avalanches,* vol. 1: *Natural phenomena,* B. Voigt (ed.), pp. 563-604. Amsterdam: Elsevier.

[79] Morgenstern, N. R. (1967), Submarine Slumping and the Initiation of Turbidity Currents, in A. F. Richards, Ed., MariPress, Urbana, 111, pp. 189-210.

[80] Mulder, T. & Cochonat, P. (1996). Classification of offshore mass movements. *Journal of Sedimentary Research*, **66**: 43-57.

[81] Murty, T. S., (1979), Submarine slide-generated water waves in Kitimat Inlet, British Columbia, *J. Gephys. Res.,* **84**, No C12, pp. 7777-7779.

[82] Murty, T. S., (2003), Tsunami wave height dependance on landslide volume, *Pure appl. Geophys*, **160**, pp. 2147–2153, DOI 10.1007/s00024-003-2423-z.

[83] Nadim F. Submarine Slides and Their Consequences.

[84] Nixon,M.F. Grozic, J.L.H. (2006). A simple model for submarine slope stability analysis with gas hydrates, *Norwegian Journal of Geology*,Vol.86,pp.309-316.Trondheim. ISSN 029-196X.

[85] Oka F. (1996). Validity and limits of the effective stress concept in geomechanics. *Mechanics of cohesive-frictional materiasl,* **Vol 1**, 219-234.

[86] Okada, Y. (1985). "Surface Deformation due to Shear and Tensile Faults in a Half-Space", *Bulletin of the Seismological Society of America*, **Vol. 75**, No. 4, pp. 1135-1154.

[87] Okal, E.A. and J. Talandier (1987). M_m: Theory of a variable-period mantle magnitude, *Geophys. Res. Letts.*, 14, pp. 847-839.

[88] Okal, E.A., G. Plafker, C.E. Synolakis, and J.C. Borrero (2003), Near-field survey of the 1946 Aleutian tsunami on Unimak and Sanak Islands, *Bull. Seismol. Soc. Amer.*, **93**, pp. 1226-1234.

[89] Okal, E.A. presentations available at: http://nctr.pmel.noaa.gov/education/ITTI/ .

[90] Panizzo A., Dalrymple R.A. (2004), SPH modeling of underwater landslide generated waves, in *Proc. Int. Conf. Coastal Eng.*, ASCE, Lisbon, Portugal.

[91] Pelinovsky, E. and A. Poplavsky (1996), Simplified model for tsunami generated by submarine landslides, *Phys. Chem. Earth*, **21**, pp. 13-17.

[92] Poulos H. G. (1988). Marine Geotechnics. Unwin Hyman Ltd, London.

[93] Prins, J.E, (1958), Characteristics of waves generated by a local disturbance, *Tans. Am. Gephys. Union,* 39(5), pp. 865-874.

[94] Putman J. A. (1949). Loss of wave energy due to percolation in a permeable sea bottom. *Trans. Am. Geophys. Union* **38**, pp. 662-666.

[95] Rahman M. S. & Layas F. M. (1985). Probabilistic analysis for wave-induced submarine landslides. *Mar. Geotech.*, **vol. 6**, pp. 99-115.

[96] Raichlen, F. & Synolakis, C. E. (2003), Runup from three dimensional sliding masses. Long Waves Symposium (ed. M. Briggs Ch. Koutitas) pp. 247-256. Salonica, Greece.

[97] Roscoe K. H., Schofield A. N. and Wroth C. P. (1958). On the yielding of soils, *Geothechnique,* **8,** pp. 22-53.

[98] Sangrey D. A., Henkel D. J. & Esrig M. I. (1969). The effective stress response of a saturated clay soil to repeated loading. *Can. Geotech. J.,* **vol. 6**, pp 241-252.

[99] Sangrey D. A., Castro G., Poulos S. J. & France . W.J. (1978). Cyclic loading of sands silts and clays. *Proceedings of the ASCE Special Conference on Earthquake Engineering and Soil Dynamics, Pasadena,* **vol. 2**, pp 836-851.

[100] Sarma, S. K. (1973), Stability Analysis of Embankments and Slopes, *Geotechnique*, **22**(3), pp. 423-433.

[101] Sarma S.K. & Jennings D.N. (1980). A dynamic pore pressure parameter. *Proc. Int. Symp. on Soils Under Cyclic and Transient Loading*, pp. 295–298.

[102] Scholz, C.H, (1982). Scaling laws for large earthquake: consequences for physical models, *Bulletin of the Seismological Society of America*, **Vol. 72**, No. 1, pp. 1-14.

[103] Seed, H.B. and Idriss, I.M. (1971), Simplified Procedure for Evaluating Soil Liquefaction Potential, *Journal of Soil Mechanics and Foundation Engineering Division*, ASCE, Vol. 97, No. SM9, pp. 1249-1273.

[104] Seed, H. B., and J. R. Booker (1976). Stabilization of potentially liquefiable sand deposits using gravel drain systems. *Earthquake Engineering Research Center, Report EERC 76-10.* University of California, Berkeley, pp. 1-34.

[105] Seed H. B. & Rahman M. S. (1978). Wave-induced pore pressures in relation to ocean floor stability of cohesionless soils. *Mar. Geotech.*, **vol. 3**, pp. 123-150.

[106] Seed, H. B. and Idriss, I. M. (1982), Ground motions and soil liquefaction during earthquakes, Earthquake Engineering Research Institute, Berkeley, CA, 134.

[107] Seed, H.B., Idriss, I.M. and Arango I. (1983), Evaluation of Liquefaction Potential using Field Performance Data, *Journal of Geotechnical Engineering*, ASCE, Vol. 109, No. 3, pp. 458- 482.

[108] Sitharam, T. G., GovindaRaju L. and A. Sridharan (2004), Dynamic properties and liquefaction potential of soils, in Special section: Geotechnics and earthquake hazards, Current Science, (87) 10, pp. 1370-1378.

[109] Skempton, A. W. (1954). The Pore Pressure Coe?cients A and B, *Geotechnique*, Institutions of Civil Engineers, Great Britain, 4, 143–147.

[110] Sleath J. F. A. (1970). Wave-induced pressures in beds of sand. *J. Hydraul. Div., ASCE* **96**, pp. 367-379.

[111] Streim, H. L. and Miloh, T. (1976), Tsunamis Induced by Submarine Slumpings o? the Coast of Israel, *Int. Hydrographic Rev.* LIII, pp. 41–55.

[112] Suhayda J. N. (1974). Surface waves and bottom sediment response. *Mar. Geotech.*, **vol. 2**, pp. 135-146.

[113] Synolakis, C.E., Liu, P., Carrier, G., and Yeh, J. (1997). Tsunamigenic seafloor deformations, *Science*, V.278 (5338), pp. 598 - 600.

[114] Synolakis, C.E., J.-P. Bardet, J.C. Borrero, H.L. Davies, E.A. Okal, E.A. Silver, S. Sweet, and D.R. Tappin (2002), The slump origin of the 1998 Papua New Guinea tsunami, *Proc. Roy. Soc.* (London), Ser. A, 458, pp. 763-789.

[115] Synolakis, C.E., (2003), Tsunami and Seiche, in *Earthquake Engineering Handbook*, edited by Chen, W–F and Scawthorn, C., CRC Press, 9–1-9–90.

[116] Synolakis, C.E., and Bernard E.N., (2006), Tsunami Science Before and after Boxing Day 2004, *Philosophical Transactions* , A 364, 2231-2265, doi: 10.1098/rsta.2006.1824.

[117] Tadepalli, S. & Synolakis, C. E. (1994), The runup of N-waves on sloping beaches. *Proc. R. Soc.* A 445, pp. 99–112.

[118] Tadepalli, S. & Synolakis, C. E. (1996), Model for the leading waves of tsunamis. *Phys. Rev. Lett.* **77**, pp.

[119] Tappin, D. R., Matsumoto, T., Watts, P., Satake, K., McMurtry, G. M., Matsuyama, M., Lafoy, Y., Tsuji, Y., Kanamatsu, T., Lus, W., Iwabuchi, Y., Yeh, H., Matsumotu, Y., Nakamura, M., Mahoi, M., Hill, P., Crook, K., Anton, L., and Walsh, J. P. (1999), Sediment slump likely caused 1998 Papua New Guinea Tsunami, *EOS, Transactions of the American Geophysical Union*, 80, pp. 329-340.2141–2144. (doi:10.1103/PhysRevLett.77.2141).

[120] Tappin, D. R., Watts, P., McMurtry, G. M., Lafoy, Y., and Matsumoto, T. (2001), The Sissano, Papua New Guinea tsunami of July 1998 – Offshore evidence on the source mechanism, *Mar. Geol.*,175, pp. 1–23.

[121] Terzaghi K. (1923). Die Berechnung des Druchlassigkeitsziffer des Tones aus dem Verlauf der hydromechanischen Spannungserscheinungen, Sitzungsber', Akad. Wiss. Men, Math.-Naturwiss.Kl.Abt.lI 132, 125-138.

[122] Terzaghi K. (1936). The shearing resistance of saturated soils. *in Proc. 1st ICSMFE*, vol. 1, pp. 54-56.

[123] Terzaghi K. (1943).Theoretical soil mechanics, John Wiley & Sons, New York, pp. 11-15.

[124] Titov, V.V., Mofjeld, H.O., Gonzlez, F.I. and Newman, J.C. (1999). Offshore Forecasting of Hawaiian Tsunamis Generated in Alaskan-Aleutian Subduction Zone, NOAA Technical Memorandum ERL PMEL-114, Pacific Marine Environmental Laboratory, Seattle, U.S.A.

[125] Titov, V.V., Gonzlez, F.I., Bernard, E.N., Eble, M.C., Mofjeld, H.O., Newman, J.C. and Venturato, A.J. (2005). Real-Time Tsunami Forecasting: Challenges and Solutions, *Natural Hazards*, **Vol. 35**, pp. 35-41.

[126] Todorovska MI, Trifunac MD (2001). Generation of tsunamis by slowly spreading uplift of the seafloor. *Soil Dynam. Earthq. Engng*, 21(2), pp. 151-167.

[127] Trehu, A. M., Ruppel C., Holland M., Dickens G. R., Torres M. E., Collett T. S., Goldberg D., Riedel M. & Schultheiss P. (2006). Hydrates in marine sediments, lessons from scientific ocean drilling, *Oceanography*, **vol. 19**, no. 4, pp. 124-142.

[128] Trifunac M.D., Hayir A. & Todorovska M.I. (2001). Near-Filed Tsunami Waveforms from Submarine Slumps and Slides, Report CE 01-01, University of Southern California.

[129] Watts, P. (1997), Water waves generated by underwater landslides, Ph.D thesis, California Institute of Technology, Pasadena.

[130] Watts, P. (1998), Wavemaker curves for tsunamis generated by underwater landslides, *J. Waterway Port Coastal Eng.*,124(3), p. 127 - 137.

[131] Watts, P., Borrero, J. C., Tappin, D. R., Bardet, J.-P., Grilli, S. T., and Synolakis, C. E. (1999), Novel simulation technique employed on the 1998 Papua New Guinea tsunami, in: Proceedings of 22nd General Assembly IUGG, Birmingham, UK JSS42, Abstract.

[132] Watts, P. (2000), Tsunami features of solid block underwater landslides, *J. Waterway Port Coastal Eng.*, 126(3), pp. 144 - 152.

[133] Watts, P., Borrero, J.C., (2001), Probability distributions of landslide tsunamis. *Proc. Int. Tsunami Symp.* 2001, Seattle, WA, pp. 697–710.

[134] Watts, P., Grilli, S.T., Tappin D.R.and G.J. Fryer (2005), Tsunami generation by submarine mass failure. II: Predictive equations and case studies, *Journal of Waterway, Port, Coastal and Ocean Engineering*, pp. 283–297.

[135] Wei, Y., Cheung, K.F., Curtis, G.D. and McCreery, C.S. (2003). Inversion Algorithm for Tsunami Forecasts, *Journal of Waterway, Port, Coastal, and Ocean Engineering*, Vol. 129, No. 2, pp. 60-69.

[136] Weiss, R., Wnnemann, K., Bahlburg, H. (2006): Numerical modeling of generation, propagation and run-up of tsunamis caused by oceanic impacts: model strategy and technical solutions, Geophysical Journal International, 167, 77-88.

[137] Wells, D. A. and K. J. Coppersmith (1994), New empirical relationships among magnitude, rupture length, rupture width, rupture area, and surface displacement, *Bulletin of the Seismological Society of America*, **Vol. 84**, No. 4, pp. 974-1002.

[138] Wiegel, R. L., (1955), Laboratory studies of gravity waves by the movement of a submerged body, *Tran. Am. Geophus. Union*, 36(5), pp. 759-774.

[139] WP/WLI (International Geotechnical Societies=UNESCO Working Party on World Landslide Inventory) (1993), Multilingual Landslide Glossary. BiTech Publishers Ltd.

[140] Wright, S. G. and E. M. Rathje (2003). Triggering mechanisms of slope instability and their relationship to earthquakes and tsunamis, *Pure app. Geophys.,* **160**, pp. 1865-1877, DOI 10.1007/s00024-003-2410-4.

[141] Wroth, C.P., (1979). Correlations of some engineering properties of soil. *In* Acta Informatica: Proceedings of International Conference on the Behaviour of Off Shore Structures, Vol. 1, pp. 121-132.

[142] Notes on the Standard Penetration Test, Advanced Engineering Geology & Geotechnics, Departement of Civil Engineering, University of Memphis, Spring 2004. (text available at: www.ce.memphis.edu/4151/Documents/SPT%20Notes.pdf)

[143] http://people.uncw.edu/grindlayn/cmgl/signific.htm

[144] http://woodshole.er.usgs.gov/project-pages/hydrates/what.html

[145] http://ceeserver.cee.cornell.edu/pll-group/t2generation.html

[146] http://neic.usgs.gov/neis/eq_depot/2004/eq_041226/neic_slav_nr.html

[147] http://www.ukgeohazards.info/pages/eng_geol/landslide_ geohazard/eng_geol_landslides_classification.htm

[148] http://wiki.offshoregeohazards.org/tiki-index.php?page=Limit+ Equilibrium+Analysis+of+Slope+Stability+Due+to+Earthquakes

[149] texthttp://earthquake.usgs.gov/learn/glossary/?term=seismic

[150] http://www.pet.hw.ac.uk/research/hydrate/hydrates_why.cfm